remote sensing

MDPI

Article

Soil Classification Maps for the Lower Tagus Valley Area, Portugal, Using Seismic, Geological, and Remote Sensing Data

João Carvalho [1,*], Ruben Dias [1], José Borges [2], Lídia Quental [1] and Bento Caldeira [2]

[1] National Laboratory for Energy and Geology, Estrada da Portela, Apartado 7586, Alfragide, 2610-999 Amadora, Portugal; ruben.dias@lneg.pt (R.D.); lidia.quental@lneg.pt (L.Q.)
[2] Physics Department of Évora University and Center for Sci-Tech Research in Earth System and Energy—CREATE, Évora University, 7004-671 Évora, Portugal; jborges@uevora.pt (J.B.)
* Correspondence: joao.carvalho@lneg.pt

Abstract: The Lower Tagus Valley (LTV) region has the highest population density in Portugal, with over 3.7 million people living in the region. It has been struck in the past by several historical earthquakes, which caused significant economic and human losses. For a proper seismic hazard evaluation, the area needs detailed V_{s30} and soil classification maps. Previously available maps are based on proxies, or an insufficient number of velocity measurements followed by coarse geological generalizations. The focus of this work is to significantly improve the available maps. For this purpose, more than 90 new S-wave seismic velocities measurements obtained from seismic refraction and seismic noise measurements, doubling the number used in previously available maps, are used to update available V_{s30} and soil classification maps. The data points are also generalized to the available geological maps using local lithostratigraphic studies and, for the first time, satellite images of this area. The results indicate that lithological and thickness changes within each geological formation prevent a simple generalization of geophysical data interpretation based solely on geological mapping. The maps presented here are the first attempt to produce maps at a scale larger than 1:1,000,000 in Portugal, with direct shear wave velocity measurements. A tentative approach to produce more detailed maps using machine learning was also carried out, presenting promising results. This approach may be used in the future to reduce the number of shear wave measurements necessary to produce detailed maps at a finer scale.

Keywords: seismic hazard; Lower Tagus Valley; V_{S30}; soil classification; seismic refraction; seismic noise; multispectral images; machine learning; lithologies

Academic Editors: Yanni Dong, Tao Chen and Chao Chen

Received: 20 February 2025
Revised: 29 March 2025
Accepted: 6 April 2025
Published: 11 April 2025

Citation: Carvalho, J.; Dias, R.; Borges, J.; Quental, L.; Caldeira, B. Soil Classification Maps for the Lower Tagus Valley Area, Portugal, Using Seismic, Geological, and Remote Sensing Data. *Remote Sens.* **2025**, *17*, 1376. https://doi.org/10.3390/rs17081376

1. Introduction

The Lower Tagus Valley (LTV) region includes the Metropolitan Area of Lisbon, representing around 2.8 million people in the city of Lisbon, the capital of Portugal, the Peninsula of Setúbal, and part of the districts of Leiria and Santarém (Figure 1), totaling more than 3.7 million inhabitants. Its central location in the country and the fact that it houses the country's capital makes the region an important crossroad of national communication routes and the host of multiple critical facilities.

The LTV region (Figure 1) has been affected by several destructive earthquakes in the past [1–5]. Two main source areas are the plate boundary, which can produce large earthquakes like the 1755 (M 8.5–9; e.g., [6]) or the 1969 (M_S 8.0; e.g., [7]) events, and the local active fault system, which very probably produced the historical earthquakes of 1341, 1531 and 1909. Though the return period for earthquakes for the individual faults is large (see, e.g., [8,9]), clusters

of earthquakes occur at a much shorter time range (a few hundreds of years) [8]. The earthquake damage mitigation and seismic hazard assessment of this region are extremely important.

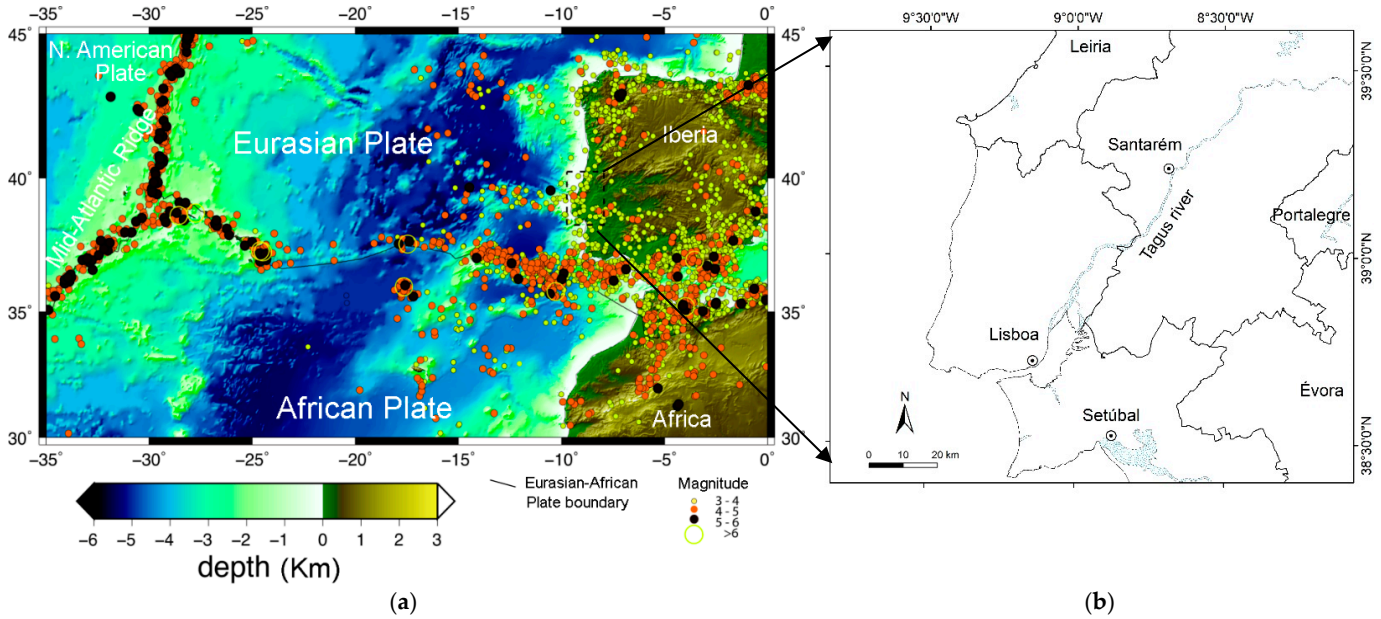

(**a**) (**b**)

Figure 1. (**a**) Location (indicated by black dashed square), seismotectonic setting of the study area, and seismicity for the period 1973–2014 after NEIC/USGS (PDE), showing earthquakes with magnitudes (mb) > 3; (**b**) district distribution in the study area.

The importance of V_{s30} and soil classification maps in site effect studies has been recognized for a long time (e.g., [10–19]) as a method for evaluating earthquake shaking and the damage potential caused by earthquakes. In the study area, the long earthquake recurrence periods make earthquake records and macro-seismic information scarce. On the other hand, instrumental recordings include only local, small to moderate earthquakes, with magnitude below 5, very rarely exceeding magnitude 6. In the last 100 years, the plate border 1969 earthquake and the local Benavente earthquake were the exceptions.

Furthermore, basin-effect studies also point to the importance of near-surface velocities and the amplification of seismic waves. In the LTV, earthquake strong-motion simulations have shown that the thick Cenozoic deposits that cover part of the LTV region, e.g., ref. [8], cause significant seismic wave amplitude amplifications [20]. For these strong-motion simulations, a velocity model with shallow information allows the use of higher frequencies and more detailed results [2,20], urging the need to estimate the near-surface properties for estimating the site effects and assessing the seismic hazard.

The above-mentioned facts reinforce the importance of producing V_{s30} and soil type classification maps for the LTV region, as they are extremely important for the design of engineering structures, and are essential to mitigating the effects of an earthquake (e.g., [16–18,21–23]). Soil classification maps, together with land and building occupancy data, can also be used to guide civil protection agencies in their plans of action in case of earthquake occurrence by estimating the level of the expected damage and casualty.

Presently available V_{s30} and soil classification maps for the study region are part of the national maps presented at scales of 1:1,000,000 or greater, and do not provide detailed information for local municipalities, see for example [10,11]. They also do not make use of direct velocity measurements and results from proxies [11] or coarse generalizations of limited data points to regional geological maps at the 1:1,000,000 scale [10,12,13]. Carvalho et al. [13] presented the first V_{s30} and soil classification maps for the study re-

gion using only 82 velocity measurements, and recognized the difficulty of generalizing/extending the data points to the geological polygons at a 1:500 K or 1:1,000,000 scale due to lithological and facies variations inside each geological formation. Therefore, these previously available maps do not take into consideration the geological complexity of the study area and present inaccuracies at regional and local scales.

Accurate V_{s30} and soil classification maps require a large number of direct S-waves measurements. To estimate S-wave velocities needed for V_{s30} and soil classification maps, several methods can be employed, such as borehole logging and seismic cone penetration tests (SCPT), seismic refraction profiles, surface wave inversion, or seismic noise (also called ambient vibrations), for example. In the scope of this work, seismic refraction and seismic noise measurements are the main source of information.

The first method requires a relatively short time for data acquisition and interpretation (thus being the cost-effective method) and can provide average values of S-wave velocity in the subsoil that can be highly variable laterally due to varying porosity, compaction, soil composition, and flow properties [24–26]. The typical problem of velocity inversion is inherent to this method, which results in the non-detection of the low-velocity layer and depth errors for the deeper layers (e.g., [27–29]). Those challenges are overcome in this work by using borehole data, standard penetration test (SPT) data, and a good lithostratigraphic control. Several authors have shown that seismic noise methods, which are also expedite methods to acquire data, can provide useful results in estimating shallow S-wave velocities for V_{S30} calculation (e.g., [13,19,30]).

In this work, we have updated the P- and S-wave velocities database to more than 170 measurements to produce a more detailed V_{s30} map and soil classification map based on Eurocode 8 for civil engineering [14]. Using the Nakamura [31] technique and the inversion of the H/V curves, 74 P- and S-wave velocity measurements were added to the V_{S30} database. Seventeen additional seismic refraction measurements in the dataset of Carvalho et al. [13] are also interpreted and used here to calculate V_{s30} and soil classification maps. Borehole information and in situ geological and lithological studies were performed to corroborate the layer depths and lithologies. P- and S-wave cross-hole measurement datasets from an engineering construction site and three other downhole measurements [31] were further appended, resulting in maps with unprecedented detail. A total of 173 S-wave and P-wave measurements were used to produce the maps in this study. The other novelty of this work is in the process used to extrapolate the velocity/soil class data points to each geological polygon. While previous work used unpublished lithological information available to the authors and in situ geological surveys, here we also used remote sensing imagery to assess further separation within each geological polygon. This separation is supported by a cross-correlation analysis between seismic, geological, and RS data, resulting in the first V_{s30} and soil classification maps with direct velocity measurements at a finer scale than 1:1,000,000 in Portugal.

Though the data points (V_{s30} measurements and estimated soil type) are generalized to the digital 1:1,000,000 scale cartography, using more detailed lithological and remote sensing data resulted in maps at a lower scale. For this generalization, more than only information from 1:50,000 scale geological maps and unpublished lithostratigraphic studies were used, as in the previous work of Carvalho et al. [13], but satellite images were also employed to confirm and improve the soil classification. Finally, a machine learning algorithm is tentatively used to perform a soil classification at a finer, local scale, trained with the RS, geological, and the initial soil classification, using the 1:1,000,000 geological cartography.

2. Geological Setting

Figure 2 shows a simplified geological map of the study area, which is located approximately 250 km from the generally E–W trending, Eurasia–Africa plate boundary. Part of the study area is the so-called Lower Tagus Basin (LTB), whose origin is related to the Pyrenean compression, and which is filled with Cenozoic deposits (Figure 2). The LTB region is surrounded by Mesozoic sediments of the Lusitanian Basin (LB) (Figure 2) to the west and by the pre-Mesozoic basement to the east (Figure 2).

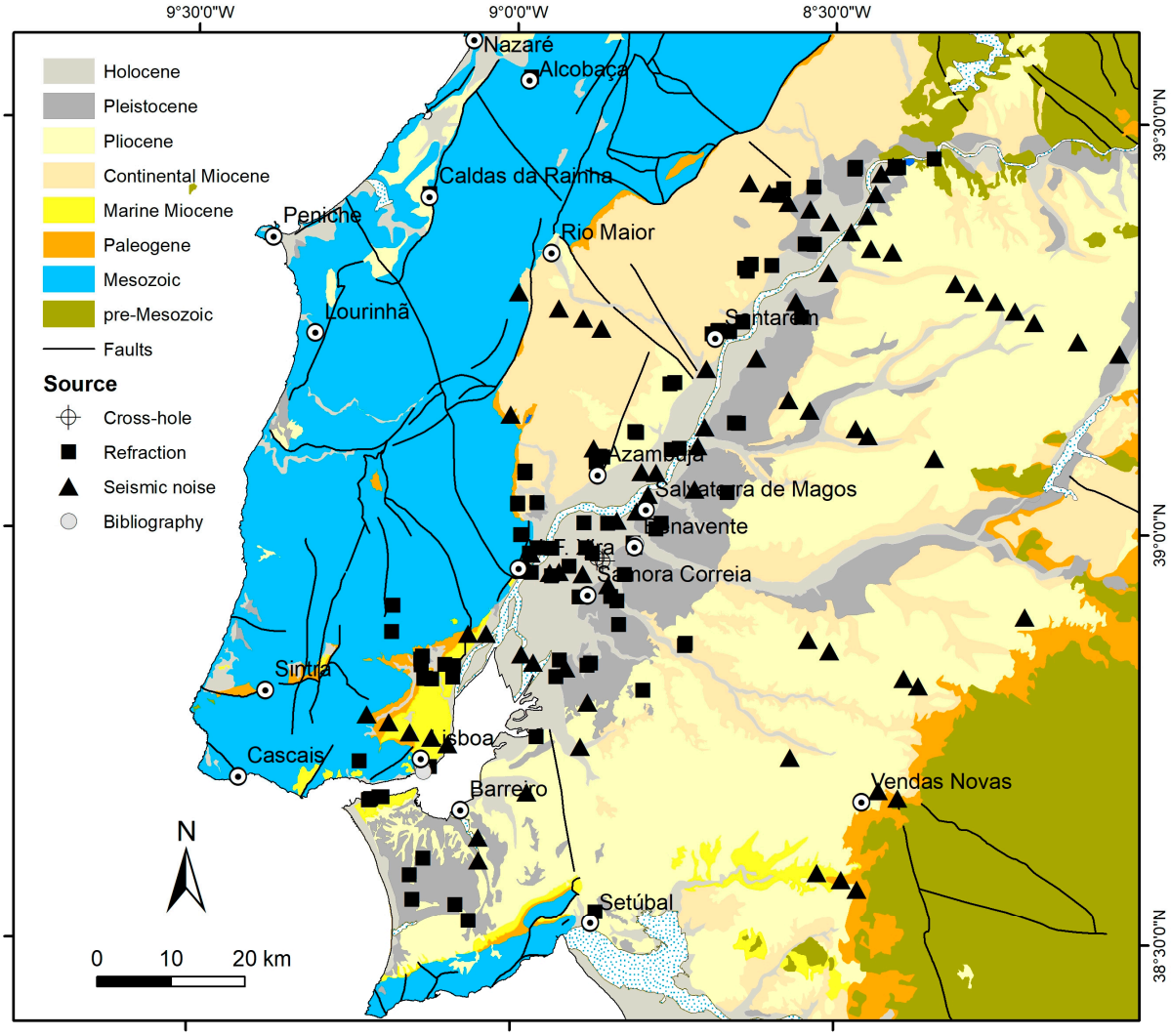

Figure 2. Simplified geological map of the study area (adapted from [32]) with the location of the 173 data points used in the present research: 94 S-wave refraction profiles (black rectangles), including 36 old P-wave profiles from which Vs was calculated, 74 seismic noise measurements (black triangles), 3 data points published by [31] (gray circles), and 2 cross-hole measurements at an engineering construction site (circled cross).

The LTV region is underlain, from a stratigraphic point of view, by a basement constituted by Paleozoic and Proterozoic metamorphic and igneous, overlain by a Meso-Cenozoic cover. Jurassic basic dykes, a Late Cretaceous intrusion (Sintra Massif), and the Volcano-Sedimentary Complex of Lisbon ([32], Figure 2) intrude the Mesozoic sedimentary cover. The lowermost deposits of the LTB, that outcrop at the borders of the basin, according to geological, well, and seismic data consist of up to 500 m thick continental Paleogene sediments (Benfica Fm. and Vale do Guizo Fm.) [33]. Paleogene sediments comprise continental siliciclastic conglomerates, consisting of clasts of quartz, quartzite, lyddite, shales

and feldspathic clasts of greenish color of Hesperian Massif, arkosic sandstones, siltstones and claystones, sometimes with nodular or crusted carbonate horizons [34]. Occasionally, Mesozoic limestone clasts appear in the conglomerates. Towards the top the formation is thinner, consisting of yellowish clays and sandstones with important carbonate accumulations, including a massive thick carbonate layer capping the Palaeogene deposits. The clay fraction is rich in paligorskite and smectite [35].

During the Miocene, over 800 m of continental and shallow-marine sediments have accumulated in depocenters [8]. Miocene geological units include: in the SW sector of LTB ten depositional sequences have been characterized, initiated by a transgressive surface and shallow marine deposits passing upwards to marls with marine microfossils and finishing with highstand progradational deposits [35]; in the central sector of LTB, the sedimentation was mainly fluvial, with the deposition of sandy-clay deposits sometimes rich in feldspars (arkoses), with pavements of clasts, and some lutites interbedded (Alcoentre Fm) of Early and Middle Miocene age. The existence of some layers with oysters suggests the penetration of brackish water to about 100 km from the current coastline (near Santarém) during eustatic high levels. This formation passes to the top, to the clay bodies, with the development of carbonated crust (Tomar Formation) and laterally into swamp and lacustrine limestones (Almoster Formation), from the Upper Miocene [34]. Almoster Formation comprises white to gray limestones; breccia structures are common, and sandy and lutite facies occur. In the clay fraction, smectite and illite predominate. The Tomar Formation consists of reddish-orange mudstones with illite and kaolinite predominance. Locally, in Rio de Moinhos, the Abrantes area has been recognized for conglomerates that correspond to alluvial deposits (probably from the late Tortonian to the Zanclean) in the SE of the foothills of the Portuguese Central Cordillera [35].

In the Pliocene, quartz-feldspathic sands (Ulme Formation) were extending from the NE to the SW sector at the Peninsula of Setúbal (Santa Marta Formation). The Pliocene units, mainly comprise sands or silty sands, yellowish to reddish in color, and with a medium to coarse texture with high amount of kaolinite and illite in the clay fraction. In the Late Pliocene, in the NE sector of the LTB, there was an increase in fluvial energy, leading to the transport and accumulation of gravels (Almeirim Formation) extending to the extant littoral coast, where they constitute a part of the Belverde Formation [35].

The Late Pliocene to Pleistocene sediments do not exceed 300 m of thickness [34]. Pleistocene fluvial terraces comprise sands and clays topped with beds of pebbles. During the Holocene, the Tagus river deposited alluvial sediments (clay, sands and pebbles).

3. Methods and Data Collected

3.1. Velocity/Depth Point Data

3.1.1. Seismic Refraction Profiles: Data Acquisition and Interpretation

The location of the seismic refraction profiles was selected to sample all the geological formations present in the study area and their distinct lithologies. The exact location of the profiles took into consideration surface geology, logistics, and the location of existing geotechnical soundings and water supply wells, as LNEG is the national repository of geological and borehole data. Surface geology and lithology were chosen using 1:50,000 geological maps and were confirmed in situ by a detailed geological survey. Neogene and Quaternary geological formations were sampled at least once, while Mesozoic and Paleozoic formations were poorly sampled, as they were generally considered of low hazard/risk. Paleozoic units were sampled only once, while mesozoic units were sampled six times, leaving many lithologies unsampled. Figure 2 shows the location of all velocity datapoints, while Table A1 in the Appendix A describes the geological formations and lithologies that were sampled.

A total of 94 locations were selected. Among these 94 profiles, included were 36 P-wave refraction profiles that were used to derive S-wave velocities, using the methodology employed by Carvalho et al. [13] (Figure 2). Additional 17 seismic refraction profiles were added in the scope of this work, acquired from engineering studies from 2016 and 2017. Profiles PENE01, PERU01, FONT01 and those named SCPCi, BANTi and SIi are used in this study to complement the previous V_{S30} refraction database (Figure 2).

In the dataset from the study by Carvalho et al. [13], a total layout length of 84 m was used to acquire most of the profiles, with 24 vertical and 24 horizontal receivers spaced 3.5 m apart. Profiles BANT01 and BANT02 used 36 m and 48 m receiver layout length due to the lack of available space, while profile SCPC01 had a total length of 107 m. For profiles SCPC02, SCPC03, BANT03, PENE01, SI01, SI06, SI08, SI11, SI12, and SI13, a total length of 96 m was used. Finally, profiles SI05 and SI07 were acquired with a 104 m length layout.

Two major problems could occur from this refraction dataset: (1) insufficient depth penetration, as V_{s30} estimation requires an investigation depth of 30 m, and (2) the typical velocity inversion and hidden-layer problems associated with the seismic refraction method (e.g., [27,28]). It is generally assumed that, depending on the velocity structure, investigation depth from the refraction method is approximately 2–10 times the receiver length (e.g., [35–40]).

Using borehole data and local geological surveys, the existence of high velocity lithologies or highly compacted layers was checked for each profile between the deepest seismic interface detected in each refraction profile and 30 m, to confirm that the required investigation depth had been reached. Borehole data were used not only to verify if 30 m investigation depth had been achieved but to also detect the possible presence of velocity inversions and constrain the refraction interpretation.

The processing and interpretation of P- and S-wave refraction data were carried out using commercial software, employing the generalized reciprocal method (GRM, [28,30]) complemented with the intercept-slope method for the stations that did not receive inverse shots, and reciprocal times could not be calculated. Data were acquired with a 0.1 ms sampling rate, as suggested by Palmer [28], using 24 vertical 50 Hz receivers, 24 40 Hz receivers, and a 5 kg hammer and plate as a source. For S-wave acquisition, a wooden beam under the wheels of a 1–5 ton jeep was hit on both sides, to avoid P-wave contamination and produce data redundancy for first break picking. A receiver spacing of 3.5 m was used, two offensive shot points, and three shot points inside the receiver layout were fired to obtain good velocity control of the shallowest layer.

Data were visualized at different scales and filtered to detect first breaks with confidence. The optimum X-Y spacing ([27,290]) was analyzed to detect possible velocity inversions, and nearby borehole data and information from the local geological survey was used as a starting model and for corroboration of the final interpretation. After assigning the first breaks to the respective refractors, an inversion to obtain a velocity model by minimizing the fit between calculated and observed travel time curves through a least-square procedure was applied. Finally, this model was compared with the model obtained from the GRM. The interpretation of the two example profiles is shown in Figure 3. More details on the acquisition and interpretation of the seismic refraction data can be found in [13]. All the Vs values obtained for this dataset are shown in the Appendix A, in Table A1.

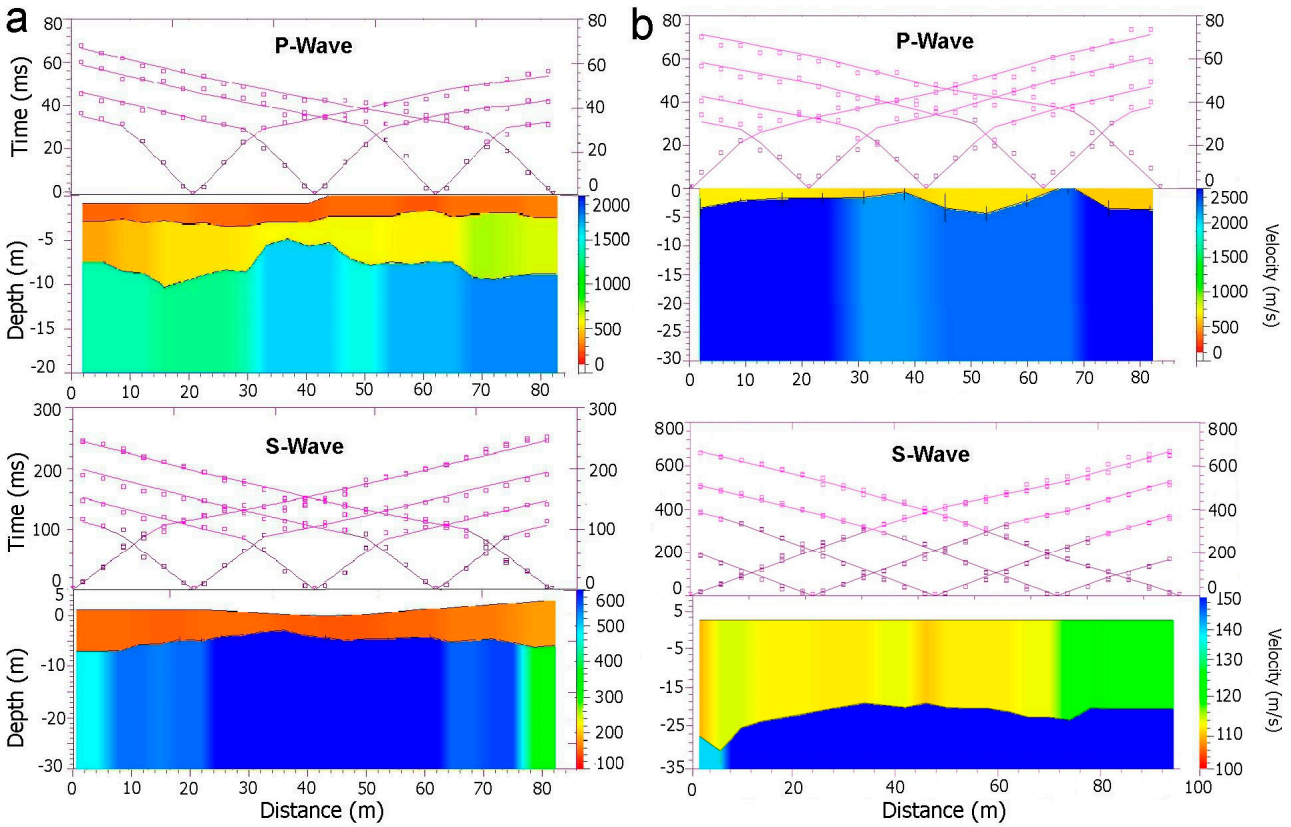

Figure 3. Examples of velocity models derived from the seismic noise data inversion and S-wave seismic refraction interpretation, located in (**a**) Banática (Barreiro) (BANT03) and (**b**) Benavente (Si11). **Top** panels in each of the 4 profiles display time–distance curves with layer interpretation. Black lines: first layer; purple lines: refractors. Squares indicate arrival times at each receiver. The **bottom** panels show the derived velocity models.

3.1.2. Seismic Noise Measurements

Previous studies [13] showed that refraction and seismic noise (SN) measurements provide very similar velocity values, despite the different frequency range sampled by each method. In this work, 73 SN measurements were acquired with Guralp CMG6TD Broadband (30 s) seismic stations. The 60 min, 3 component records, collected along the profiles were clean from spikes or other transient events and processed in order to obtain the horizontal-to-vertical spectral ratio (H/V) [31].

This observed H/V spectral curves are submitted to an inversion process using the software ModelHVSR (Ver. 3.3) [41] to obtain the 1D Vs model under each employed station. In the inversion process, it is assumed that each individual point of the profile has a 1D horizontally layered structure below, with fixed depth of interfaces obtained from borehole information. Input parameters for the inversion procedure are S-wave and P-wave velocities and density. Initial velocities from nearby velocity measurements for similar lithology and formation, together with borehole data, were used as starting models, to avoid conversion of the algorithm to local minimum. As density data are unavailable, we assume for each layer a density versus V_P given by the Gardner's relationship [42] and we admit a V_P/V_S (or Poisson ratio) versus Vp given by the Brocher's empirical law [43]. Both V_P/V_S ratios and a density has been submitted to a perturbation window of 25% in order to achieve the best solution. Calculated curves are then compared with observed curves until a good match between the two is found. An example of a final inversion result and respective velocity model obtained for point 4_4 (see Table A1) is shown in Figure 4. A

more detailed explanation of the method used can be found in [21]. The Vs values obtained for this dataset are also shown in Table A1.

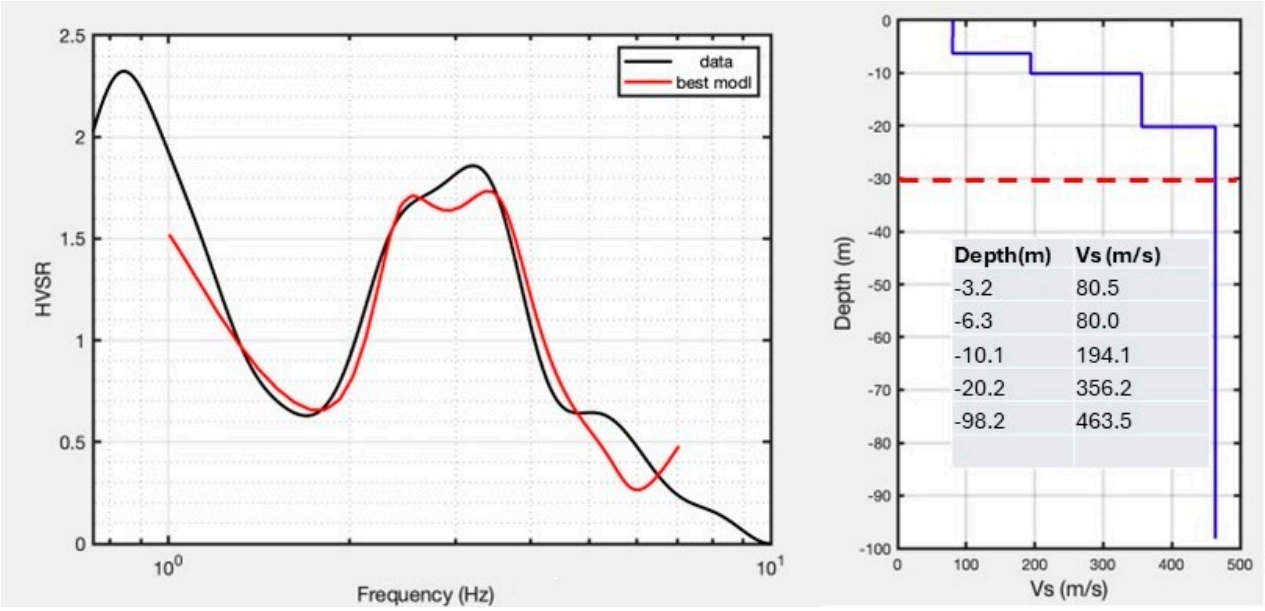

Figure 4. Example of inversion procedure for seismic noise point 4_4, acquired over alluvium (see Table A1). Left: inversion results (field curve in black, theoretical curve from best fit model in red); right: velocity model resultant from the inversion (blue line). Dashed line indicates depth limit used for V_{S30} calculation.

3.1.3. Cross-Hole and Other Authors Datasets

Two cross-hole VS measurements in the Benavente area, which were carried out for engineering construction, and three geotechnical boreholes acquired in downtown Lisbon [31], were also used in this study. Cross-hole data were acquired with a Geotomographie equipment, a multicomponent receiver BGK-7 and a StrataView R-24 seismic acquisition system till a depth of 57 m. The VS downtown Lisbon borehole measurements were estimated from the NSPT using empirical relationships that were calibrated by ambient vibration (AV) analysis (H/V curves). From the published VS by [31], Vs_{30} and soil types in three locations in downtown Lisbon (north, center and south) were calculated. The Vs values range between 175 and 240 m/s, and the soil classes are C and D. These data points have been integrated in Table A1.

3.2. Geology and Velocity Analysis

Table 1 shows the average V_{S30}, respective standard deviations, and the number of samples obtained for each of the Cenozoic and basement (pre-Cenozoic) formations. Basement includes sedimentary, metamorphic and igneous formations of Cretaceous to pre-Cambrian age. For a full description of Lisbon Miocene formations see the Geological Setting section. The basement formations have been poorly sampled, and standard deviation was often not calculated. Note that for these data, the first layer is not considered if its thickness is less than 1 m, as in these cases the surficial layer is constituted by loose soil, not representative of the respective geological formation velocity. Nevertheless, note the abnormal low velocity (compared to expected values) for the Jurassic/Cretaceous sandstones of Abadia Fm. and Almargem Fm. (profiles PS43 and RM_MG_1, see Table A1), possibly due to weathering.

Table 1. Average V_{s30} values and respective standard deviations for the geological formations and respective lithologies of the study area (according to the 1:50 k scale maps) that have more than 1 data point, using data in Table A1.

Geological Formation	Main Lithologies	Age	Average V_{s30} (m/s)	Std Dev (m/s)	N Points
Alluvium	clays	Holocene	287	259	34
Alluvium	sands, gravels	Holocene	313	259	32
Undif. sands and gravels	sands, gravels	Pleistocene	454	193	27
Fluvial terrace deposits	sands, gravel	Pleistocene	452	151	14
Porto Concelho Fm.	sands, marls	Pleistocene	282	-	1
Ulme Fm.	sandstones, gravels	Pliocene	386	124	25
Lisbon, Miocene: Banco Real Fm., Musgueira Limestones, etc., Undif. Alcoentre Fm. and Tomar clays	limestones, sandstones, claystones often w/carbonate crusts	Miocene	469	330	25
Undif. Alcoentre Fm. and Tomar Clays, Lisbon Miocene: Areias da Quinta do Bacalhau, Argilas Forno do Tijoplo, etc.	sandstones, claystones, clayey sandstones	Miocene	435	179	16
Benfica Fm., Vale do Guizo Fm., Monsanto Fm.	claystones, sandstones, gravels, w/carbonate crusts	Paleogene	526	262	5
Lisbon Volcanic Complex	weathered basalts	Cretaceous	523	81	3
Almargem Fm.	sandstones, mudstones	Cretaceous	268	-	1
Freixial, Sobral e Arranhó	sandstones, limestones	Jurassic	1077	-	1
Abadia Fm.	claystones, sandstones	Jurassic	536	-	1
Basement	gneisses	Precambrian	1240	-	1

3.3. Point Data Generalization to V_{s30} and Soil Classification Maps Using Geological and Remote Sensing Information

All shear wave velocities used in this research are presented in Table A1, in the Appendix A, organized by geological units. The estimated V_S values for all profiles are consistent with measurements carried out in similar shallow sediments using seismic refraction data (e.g., [44–47]). The estimated V_s ranges are approximately 60–690 m/s and 140–1650 ms/s for the first and second layer, respectively.

To calculate V_{s30} values at each measurement site, the formula by Borcherdt [15] was used, while the soil class was based on the revised Eurocode 8 [14]. The criteria used in this research are shown in Table 2. NSPT was not included in the original soil classification presented by Penelis [16], but it has been considered in the revised Eurocode soil type classification [14] and has been incorporated in the soil classification presented here for most of the data points.

To produce V_{s30} and soil classification maps of the study region, the sparse data points had to be extended/generalized to each geological polygon by providing seismic information (V_{s30} and soil type) to the available geological digital vector maps. Presently, geological vector maps at the 1:25,000 and 1:1,000,000 scale were available for this task. The 1:1,000,000 vector maps were used in this paper due to practical and visibility reasons. However, digital geological raster maps at the 1:50,000 scale and the 1:25,000 scales vector maps were used for geological and lithological information. Several methods are available to generalize velocity/soil type data points to geological/lithological polygons: a geological-lithological approach (e.g., [48–52]), the topographic slope method [53], or through a statistical analysis [10].

The study area incorporates a vast region of flat agricultural plains, where important V_s variations have been found and, therefore, the topographic slope method is not appropriate.

A statistical approach does not take into consideration the importance of lithological information of the location of a direct V_s measurement and is used when the number of available direct measurements is low (e.g., [10,11]). Here, a geologically based approach was chosen, as lithostratigraphic maps at various scales exist at the national geological survey (LNEG) and was available to the authors. Furthermore, and as stated above, local, detailed geological surveys were carried out at each profile site, which ensured that the approach could be used successfully.

Table 2. Soil classification as defined in Eurocode 8 [14]. Vs: S-wave velocity. N_{SPT}: N value from the standard penetration test (SPT).

Ground Type	Description of Stratigraphic Profile	V_{S30} (m/s)	NSPT (Blows/30 cm)
A	Rock or other rock-like geologic formation, including at most 5 m of weaker material at the surface	>800 m/s	-
B	Deposits of very dense sand, gravel or very stiff clay, at least several tens of meters in thickness, characterized by a gradual increase in mechanical properties with depth	360–800	>50
C	Deposits of dense or medium-dense sand, gravel or very stiff clay, with thickness from several tens to many hundreds of meters	180–360	15–50
D	Deposits of loose-to-medium cohesionless soil (with or without soft cohesive layers), or of predominantly soft-to-firm cohesive soil	<180	<15
E	Soil profile consisting of a surface alluvium layer with values of type C or D and thickness varying between about 5 m and 20 m, underlain by stiffer material with V_S > 800 m/s		
S_1	Deposits containing a layer, which is at least 10 m thick, of soft clays/silts with a high plasticity index (PI > 40) and high-water content	<100 (indicative)	-
S_2	Deposits of liquefiable soils, made of sensitive clays, or any other soil profile not included in types A–E or S_1		

LNEG is also the national repository of borehole data. Geological cores, geophysical logs, and SPT data reports are available and were geo-referenced and integrated in a GIS together with other geological data. Not only was the closest borehole to the seismic profile used, but also multiple other available boreholes in the area were utilized, which, together with the detailed geological surveys carried out, gave us a better idea of the sub-surface geology of the region around each profile and of possible lateral variations in layer-thicknesses and lithologies. Borehole data were used to corroborate seismic interpretation. If the initial velocity model was different than the average structure observed in borehole data, the velocity model was revised, unless borehole data showed strong variations. Therefore, when the boreholes were located several hundred meters from the profile location, we avoided possible lateral lithological variations and ensured adequate lithological control, establishing, for example, until which depth the outcropping geological formation was present.

Each geographically distinct outcrop of a particular geological unit (hereafter called a geological polygon or, simply, polygon) was therefore filled in using an average of the available data points (V_{S30}) inside that polygon, with no interpolations or extrapolations for other polygons. No data were discarded, even if velocity outliers were present. A few outliers in some geological formations were present, but as we have good confidence in the velocity models due to available borehole data and detailed geological survey carried out at each site, we assume that these are outlier are not caused by interpretation errors but rather local geological conditions. For each polygon, unpublished geological and lithological information was used together with digital geological cartographic data in scales from 1:50,000 to 1:500,000 to fill it in. Satellite images were also used to check if each of these polygons contained unmapped different lithologies.

Remote Sensing (RS) information from the Copernicus Sentinel-2 mission was the ancillary source used to verify if each polygon could be separated into more polygons but only if this separation was also supported by geological/lithological information and if corresponded to distinct classes of VS30. The multispectral Sentinel-2 images at level 2A, available at Copernicus Data Space Ecosystem https://dataspace.copernicus.eu/ (accessed on 20 January 2025), captured for year 2020, were mosaiced for the study area and resampled to 10 m pixel size. In 12 bands, excluding the water vapor band, a multivariate data analysis was performed using Principal Component Analysis (PCA) [54] to compress the information based in a covariance matrix in components that can explain and synthetize the spectral information (Figure 5a). The similar, but more advanced, Minimum Noise Fraction (MNF) algorithm [55], as implemented in ENVI 6.1 software, was also tested (Figure 5b). RS data responds to distinct surface properties such as vegetation coverage, soil type or other very superficial ground properties.

V_{S30} is a parameter that includes information up to 30 m depth and it is not clear how RS data can be correlated with it. The fact is that several distinct RS polygons in the study area could be associated with different VS30 classes. Possibly, some RS properties are related to soil type, grain size, or cementation, and in areas where surface geology extends at least to a few tens of meters, RS properties can be used to distinguish between distinct VS30 classes. For example, the alluvial covered area, where generally the thickness of Holocene sediments reaches 40–50 m, is clearly evidenced in the RS images.

Independently of the nature of the RS data response, using also geological/lithological and V_{S30} value information, several of the 1:1,000,000 geological polygons were subdivided into two or more polygons, and therefore the map presented here contains information at a larger scale than 1:1,000,000.

Most of the geological polygons contained several data points (V_{S30} measurements) within them. However, not all geographically distinct geological polygons of the same geological formation (e.g., the Holocene alluvium has different outcrops across the study area) were sampled. For at least one of the polygons of a certain geological formation, all the lithologies that incorporate this geological formation were sampled. This was ensured for all the different Cenozoic geological formations that outcrop in the study area. In other words, we have sampled all Cenozoic lithologies.

When several (more than 2) data points were present inside a particular polygon, we averaged the V_{s30}/soil-type value/class values. If only one or two V_{s30} measurements were available for a certain polygon, we averaged the V_{s30} values from neighboring polygons. If no V_{s30} data point was available for a particular polygon, we used the average of adjacent polygons with the same lithology/geology. If no polygons with the same lithology/geology existed nearby, the polygon was colored gray in the maps. Using this approach, a V_{s30} map was produced using the 1:1,000,000 scale geological map [32].

Next, using the same approach, the soil classification map was elaborated based on the revision of Eurocode 8 ([14], Table 2). For this purpose, additional information based on other studies was used to complete the soil type classification map. A few previous reports were used to locate areas where liquefaction had occurred and S2 type soils were identified ([1,56–60]; see next section).

Post-Paleogene geological formations in the study area, which theoretically present the highest hazard, have all been sampled in this work. Paleogene formations, which according to velocity information gathered in other parts of the globe should present a very low hazard (e.g., [61–63]), were only partially sampled. Mesozoic and Pre-Mesozoic formations are assumed to have a low or very low hazard. Nevertheless, a few Jurassic and Cretaceous igneous and sedimentary formations, together with a Pre-Mesozoic metamorphic formation, were sampled inside the study area to check if the weathered layer could present low Vs values and most

hazardous soil classes of type D or E, as defined in the EC8. Information available from other sites outside the study area in Mesozoic and Pre-Mesozoic formations was also used for this purpose. This information is provided in Table 3. It was verified that some Mesozoic lithologies may pertain to soil class B, or even class C. The lack of lithological maps did not allow to separate these areas in the current V_{S30} and soil type maps. Using RS data, it was also not possible to distinguish these lithologies. Therefore, in the V_{s30} map (Figure 6) the Mesozoic and Pre-Mesozoic outcropping areas were mapped with average values as usual or colored gray if velocity measurements were not available at least in adjacent polygons. However, in the soil classification maps, it was assumed that the generality of these Mesozoic/Pre-Mesozoic areas is of class A, although some localized areas may fall into other categories, as indicated by some velocity measures carried out in the scope of this work. The lack of velocity measurements prevents a detailed mapping of these areas and will be the focus of future research.

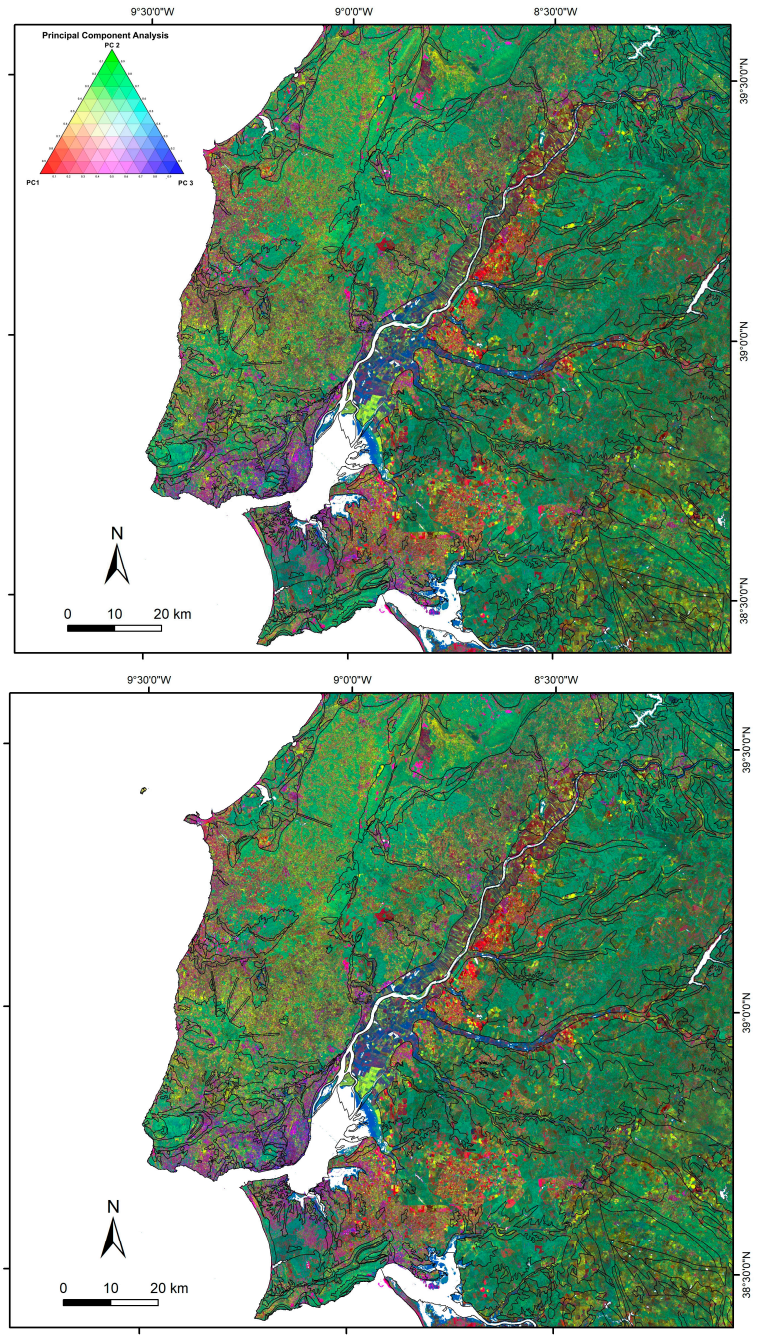

(**a**)

Figure 5. *Cont.*

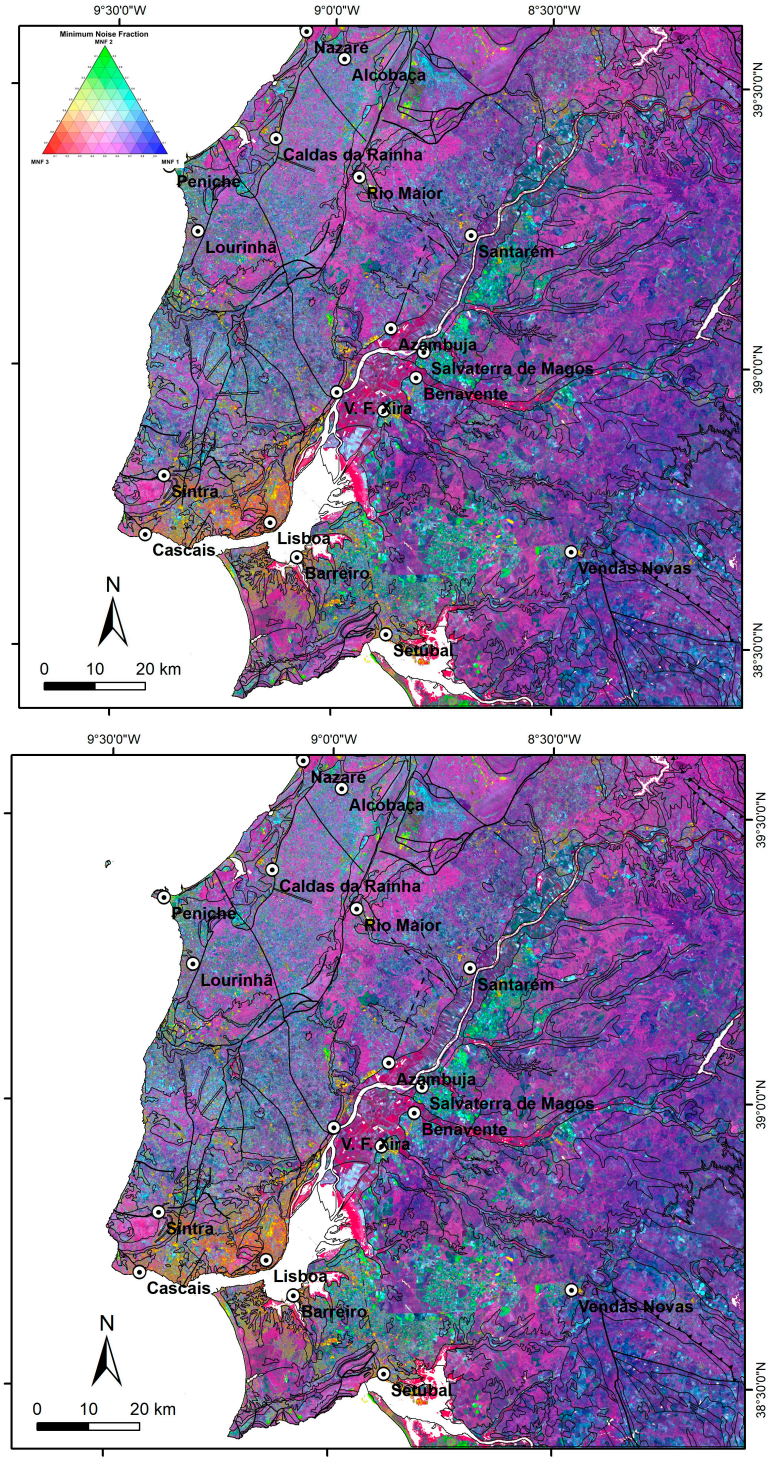

(**b**)

Figure 5. Multivariate analysis of Copernicus Sentinel 2 images used to find differentiation with the 1:1,000,000 scale geological polygons compatible with velocity information. Geological contours of the 1:1,000,000 geological map are overlaid [32]. (**a**) Principal Component Analysis, RGB: PC1; PC2; PC3; (**b**) Minimum Noise Fraction, RGB: MNF3, MNF2, MNF1.

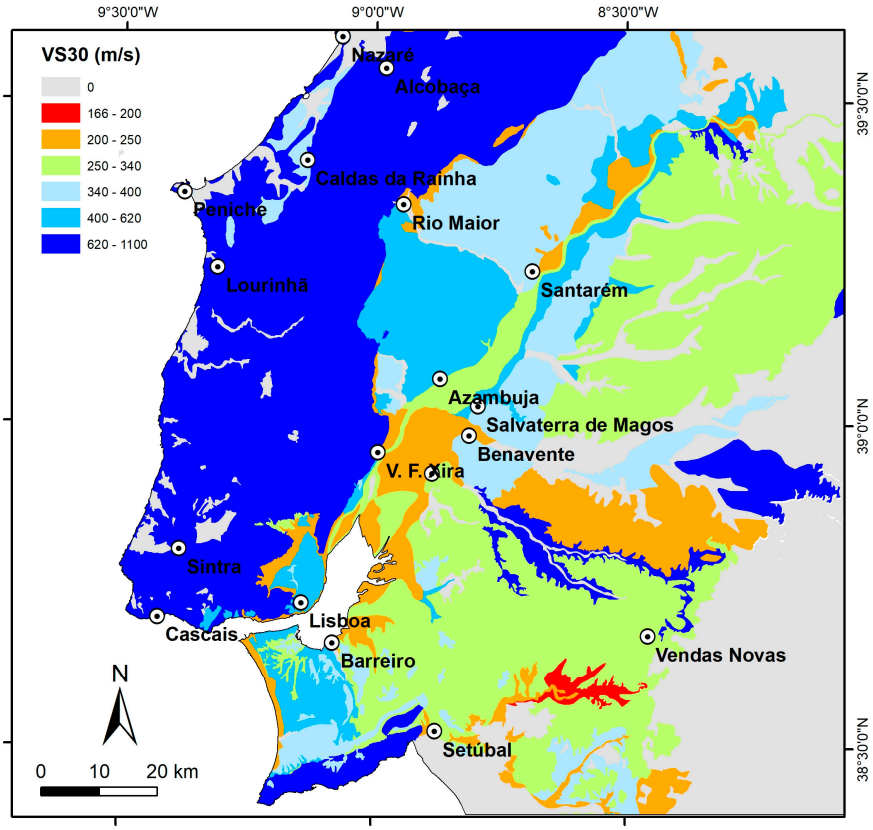

Figure 6. V_{s30} map produced for the study area. Data points are generalized/extended to a geological map at 1:1,000,000 scale [32], utilizing 1:50,000 scale geological maps and remote sensing data, resulting in the subdivision of the 1:1,000,000 geological polygons. 0: areas not sampled in this work.

Table 3. Average V_{s30} values and soil class for several data points acquired outside the study area over Paleozoic, Mesozoic, or igneous rocks and therefore not included in Table A1, highlighting the need to acquire more data over these formations, which are generally assumed to present very low hazard.

Geological Formation	Main Lithology	Age	V_{S30} (m/s)	Soil Class
Monchique Igneous Complex	Sienites	Cretaceous	657	B
$J_{3\text{-}4}$	Marls and limestones	Upper Jurassic	749	B
J_3	Marls	Upper Jurassic	1002	A
J_1	Dolomites	Lower Jurassic	1360	A
Silves Fm.	Sandstones	Triassic	999	A
Beja Igneous Complex	Gabbro	Carboniferous	839	A
Mértola Fm.	Turbidites and conglomerates	Carboniferous	1436	A
Mira Fm.	Turbidites	Carboniferous	1582	A
Brejeira Fm.	Turbidites	Carboniferous	885	A
Brejeira Fm.	Turbidites	Carboniferous	489	B
Mértola Fm.	Turbidites	Carboniferous	1375	A
Mértola Fm.	Turbidites	Carboniferous	1236	A
Terena Fm.	Turbidites	Devonian	1882	A
Paragneisses	Paragneisses	Cambrian-Ordovician	784	B

3.4. Point Data Generalization to V_{s30} and Soil Classification Maps Using AI Techniques

Despite the larger shear wave dataset measurements used here, when compared with previous works, the number of measurements still needs to be much increased to allow the generation of hazard maps at a finer scale with interest to urban planning and risk mitigation. Therefore, while these measurements are not available, we decided to implement a tentative approach to produce maps at a fine scale using artificial intelligence

techniques. For this purpose, we trained a random forest classifier, known for being robust and effective [64,65]. The input data were the RS results of the 4 factors of MNF in Figure 5b, and the training data were information of the 173 data points of Figure 2 assigned to the soil classification obtained and presented in Figure 6. The Eurocode 8 classes were balanced, the outliers were excluded, and the number of predictors were tested and settled to a standard 100 estimators or decision trees.

4. Results

The V_{s30} map produced is shown in Figure 6, while the soil classification is presented in Figure 7, and the ML random forest classification in Figure 8. The following analysis of the V_{s30} and soil classification maps was carried out using satellite images and data from the 2021 governmental Population and Housing Censuses (CENSOS). The observation of figure's 6 V_{s30} map shows that the region east of the Tagus river course, southwestwards of Salvaterra de Magos city, presents the lowest V_{s30} values, below 200 m/s. Alluvium deposited during the Holocene completely covers the region (compare Figures 2 and 6), where the water table depth averages 1 or 2 m. The alluvial unconsolidated sediments thickness is around 40–50 m, and the low V_{s30} values are therefore not surprising. V_{s30} values in the region vary by 101–301 m/s, but only two data points (V_{s30} measurements) present V_{s30} values above 200 m/s. In the first few meters, shear wave velocity (Vs) can be as low as about 20 m/s. The soil type of this region, presently an agricultural and pastoral area, is of class D, the only one of this type in the study area. During some historical earthquakes, such as the 1909 Benavente earthquake [5,56], the 1755 and 1531 Lisbon earthquake [1,58,59], and the 1858 Setúbal earthquake [60], liquefaction has been reported at several sites in this region (Figure 6). Note that the area may also be classified as S1 soil type because, according to borehole and trench data, the alluvium soils here are often composed of clays and silts with a high degree of plasticity and water content. The area is crossed by an important highway (A10), supported by pillars 10 m above the ground.

The next V_{s30} class, 200–260 m/s, also corresponds in part to alluvial sediments, but relatively higher V_{s30} values are observed due to the decrease in the alluvial thickness and the presence of more competent Miocene or Jurassic units beneath. This is the case of the alluvial cover around central Lisbon (north of Lisbon in Loures council), and the margins of the Tagus NNE of Vila Franca de Xira city, northeast of district capital Santarém and northeast of Salvaterra de Magos, on the other bank of the Tagus. However, in the largest part of the area occupied by this class outcrop mostly Pliocene sediments, at the western margin of the Tagus, north of Vendas Novas and east of Benavente, in an area occupied by multiple villages. The remaining area of this class outcrops some Miocene and Paleogene units, south and west of Vendas Novas.

All these areas are of soil type C and present and intermediate hazard, except the narrow band of alluvium south of Lisbon, close to the Tagus estuary. The regions of Santarém and V. F. de Xira are inhabited by approximately 200,000 people, around the same number of inhabitants in the peripherical areas of the council of Lisbon (Loures council) that are covered by this soil type and V_{s30} classes. It is important to mention that in the present work, the alluvial sediments of Loures were sampled twice by seismic refraction profiles (profiles TOJ1 and PS40). The V_{s30} value found at TOJ1 is about 150 m/s and falls into soil type S1 but at the other site, close to the Pleistocene outcrop where alluvial thickness is less, V_{s30} value is 296 m/s, increasing the average V_{s30} of this polygon. This means that very possibly this area of high-density population has its seismic hazard underestimated.

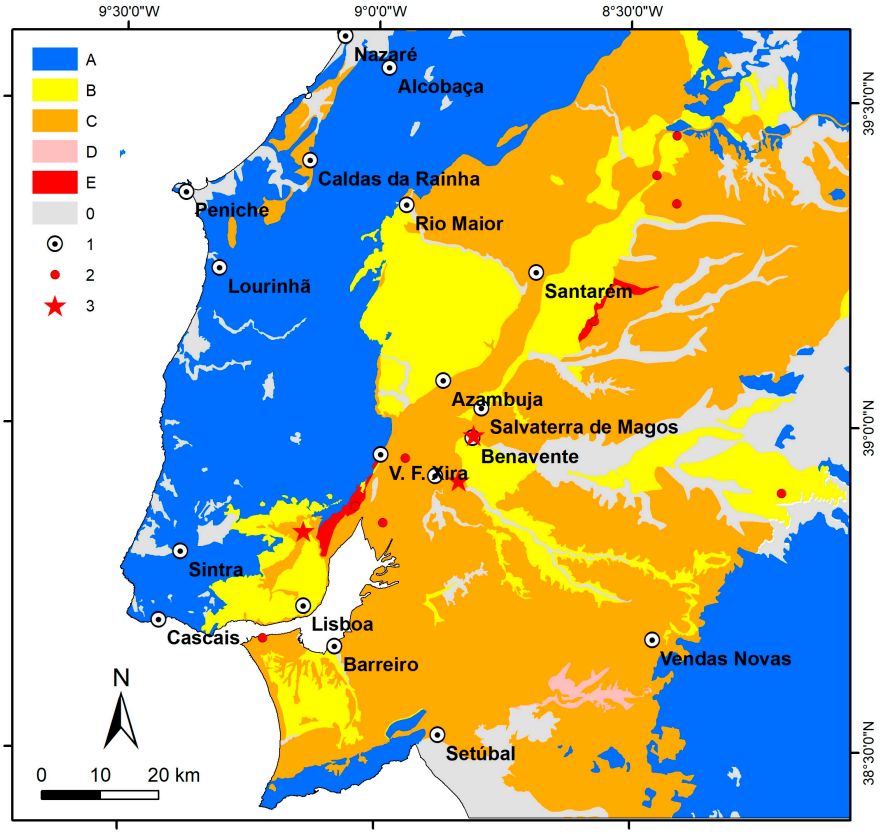

Figure 7. Soil type map based on the Eurocode 8 classification [14]. Data points are generalized/extended to a geological map at 1:1,000,000 scale [32], utilizing 1:25,000, 1:50,000 scale geological maps and remote sensing information. 0: areas not sampled in this work; 1: municipalities; 2: sites where liquefaction has been historically reported; 3: data point with E type soil class, but sited inside a geological polygon with a lower seismic hazard (soil type B or C).

The alluvial sediments in central Lisbon close to the river Tagus are also expected to have a high risk and, as stated above, have been the focus of a detailed work in the past [31]. Closer to the Tagus river, the water table is shallower, and we may find again S1 or S2 type soils. Several cross-hole and surface wave measurements have been acquired in the alluvium in the city of Lisbon and the surrounding areas [31] but only average values have been published and it was only possible to estimate V_{s30} or soil type for three data points in downtown. V_{s30} values range from 170 to 240 m/s and the soil type is class C or class D but the shear wave velocities at the other sites are like the ones known in downtown Lisbon, and they point also to soils of class C or D or S1, when the water table is shallower. The only direct measurement we had available in this area supplied a V_{s30} value of 240 m/s and classified as soil type C. Therefore, the average V_{s30} falls into class 200–250 m/s and soil type class C, the class adopted in this work but some areas of S1 type can be expected, and further measurement should be carried out here.

The next V_{s30} class, 250–340 m/s, occupies a large area in the south of the study area, east of Barreiro and west of Vendas Novas. The area is classified as C soil type and Pliocene sediments outcrop, but most of the region has little human occupation or important structures, except for the areas around the cities mentioned. The municipality of Barreiro has approximately 78,000 citizens, while Vendas Novas has a population of 11,000. On the same bank of the Tagus, two small areas in the north of the study area are also present but with no important human occupation. On the eastern bank of the Tagus, this class extends from the city of Azambuja, in the south, to the capital district Santarém, and corresponds geologically to alluvium. Besides the two cities, other small cities settle

in this area, representing a total population of approximately 100,000. The area has been classified as soil type C, like the other areas of this V_{s30} class.

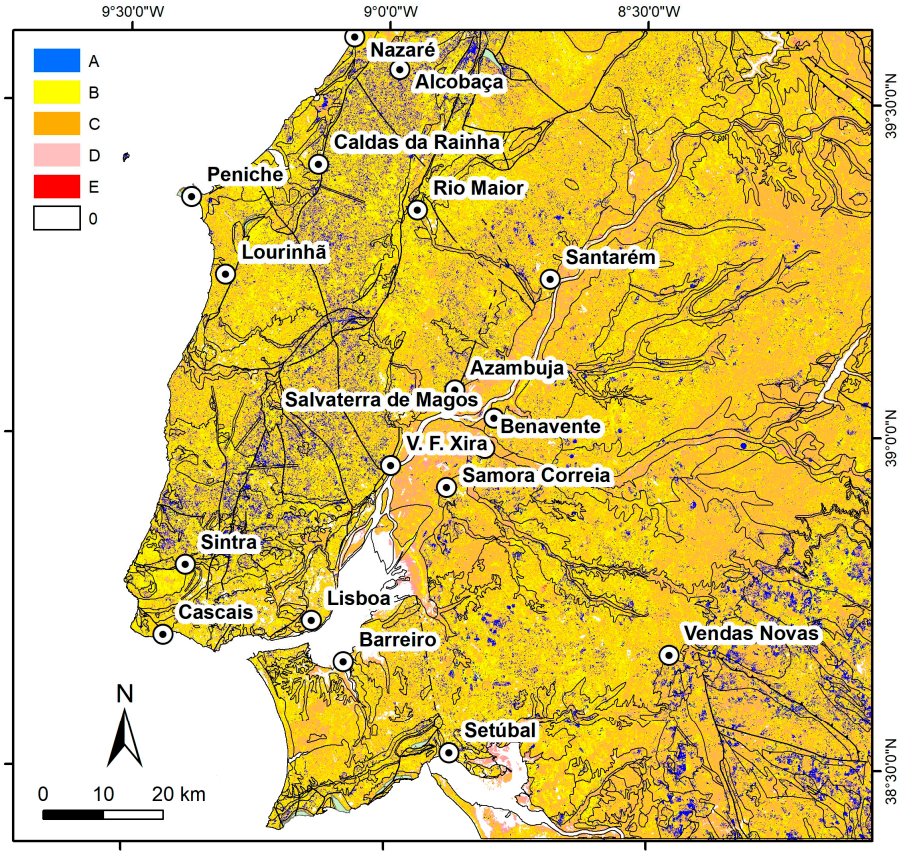

Figure 8. Soil type map produced by a machine learning random forest classification, using the Eurocode 8 classification [14] shown in Figure 6, the 173-point measurements in Figure 2, and Minimum Noise Fraction remote sensing data, presented in Figure 5b.

The 340–400 m/s class, which still presents a moderate hazard, is geographically spread throughout the study area on both banks of the river Tagus. South of the Tagus, this class is represented in areas where Pleistocene units outcrop: in the Peninsula of Setúbal, west of the district capital of the same name, in an area where several small villages are present, and in an NNE oriented band encompassing the cities of Samora Correia, Benavente and Salvaterra de Magos, the area where the 1909 Benavente earthquake caused the greatest destruction, with populations of approximately 51,000, and also the municipalities of Almeirim, Alpiarça and Chamusca, totaling 28,000 inhabitants. In the Setúbal Peninsula, this class occupies the urban region west of Barreiro, including the cities of Almada, Amora, Seixal and the villages around Costa da Caparica, a summer beach destiny for the greater Lisbon, totaling around 340,000 people. All the areas are classified as type C soil. The last region occupied by this class on this side of the Tagus is an approximately WSW-ENE band, in a narrow agricultural area around a Tagus river tributary and in the south of the study area, in a few, small, scattered terrains of soil class C, with little human occupancy.

North of the Tagus, the class is present in two regions: (i) the NNE oriented strip occupied by Miocene continental deposits, classified as of soil type B, extending from a little north of Vila Franca de Xira till the northern end of the study area, and (ii) in the northwestern part of the study area, close to the coast line around the city of Caldas da Raínha, which has a population of 50,000, where several small-sized Pliocene sediments

and alluvial deposits outcrop; all these small areas have been classified as soil type C or as unknown, once many outcrops have not been sampled.

The next class, with values ranging 400–620 m/s, exists mostly in the northern bank of the Tagus, except in a small region south of Lisbon, in the municipality of Almada, central area of Lisbon has more than 1,000,000 inhabitants, while the region between Azambuja and Santarém, that incorporates the municipalities of Cartaxo and Azambuja, totaling a population of more than 45,000.

Next, the V_{s30} class with a higher velocity (>620 m/s) generally corresponds, as expected, to the oldest (Mesozoic and Pre-Mesozoic), more compact geological formations. The exception is the narrow, elongated area excavated by a tributary of the Tagus river between Samora Correia and Vendas Novas, where continental Miocene deposits outcrop. This area has been classified as soil type B in Figure 7. The heavily populated area between Lisbon, Sintra, and Cascais, has also been classified as soil type B. It corresponds to the outcrop of the cretaceous Volcanic Complex of Lisbon, constituted by solid basalt and pyroclastic sediments. Only three velocity measurements are available in this area, and in spite of the fact that its average V_{s30} value is high (607 m/s), one of the three measurements presents relatively low seismic velocities (CNX29, see Table A1) that resulted in soil type C. Therefore, this area needs more measurements for a proper evaluation.

The same thing can be said for other units of Mesozoic age in the northern bank of the Tagus and in the Peninsula of Setúbal west of this city, all falling into this V_{s30} class and of soil type A. Sedimentary Cretaceous end Jurassic formations occupy a large part of the study area and have been sampled only three times (Table A1). One of the measurements presented a high (998 m/s) V_{s30} value but the two other measurements presented values of 307 m/s and 221 m/s and fell into soil type class C. Nevertheless, the area presented an average V_{s30} value of 521 m/s and has been classified as A soil type because, according to other measurements performed in similar geological formations and lithologies located nearby but outside the study area (Table 3), high V_{s30} values and soil class type A were found. We have therefore assumed these geological formations in the study area were poorly sampled. However, we note that another two measurements in Mesozoic formations outside the study area (Table 3) do present lower V_{s30} values and soil type B, reinforcing the need to carry more measurement in this area.

At last, Pre-Mesozoic rocks were only sampled once within the study area (see Table A1), and for this reason were not classified in the V_{s30} map, except for this outcrop, which has a V_{s30} value of 720 m/s and soil type B. In the soil classification map of Figure 7, they were attributed with class A, based on the data acquired in southern Portugal over Pre-Mesozoic outcrops composed by similar lithologies (Table 3). Among the nine measurements made outside the study area over Pre-Mesozoic formations, only at two places soil type B was found and V_{s30} values < 800 m/s, possibly due to weathering, signifying that these units do indeed present low to very low seismic hazard.

It should also be noted that a large part of the study area that has been classified as soil type C has several individual locations where class E has been obtained. These class E locations are pointed in Figure 7. Though the average V_{s30} value makes the area fall into soil type C, the existence of several points of class E, the fact that the region has been the scenery of a destructive earthquake (1909 Benavente) and its large population (>1,000,000) reinforce the need to map this area more accurately.

5. Discussion

Several points should be kept in mind in the analysis of the V_{s30} and soil classification maps produced in this work. V_{S30} values include velocities sampling vertically different lithologies and geological formations and, due to unmapped lithologi-

cal/velocity/thickness lateral variations inside a geological formation or a particular lithology, it cannot be expected that a certain geological formation is represented by a single V_{s30} or soil class. Each geological formation is therefore usually characterized by different V_{S30} classes or soil types, and of course, different geological formations may fall in the same V_{s30} or soil type class.

Table 1 presents average V_{s30} values and the respective standard deviation for each geological formation in the study area. The alluvium, Miocene formations containing carbonates, and the basement have clearly separable V_{s30} values, while Miocene siliciclastic units, Pliocene, and Pleistocene formations show overlapping shear wave seismic velocities. Standard deviations shown in Table 1 demonstrate that Vs and V_{s30} values for each geological formation have relatively large variations, depending on lithology and layer thicknesses and other factors like clay content, grain size, etc., (e.g., [62]) and according to the geographical position within the study area.

Some geological formations have larger standard deviations, such as Paleogene, Miocene, and Holocene formations, but this is not due to a lesser confidence in the data, it is rather the result of their lithological composition that shows a greater diversity. For pre-Cenozoic formations, which were poorly sampled, standard deviations could not be calculated. Looking at data collected outside the study area for these formations (Table 3), they may also present large standard deviations when more data are gathered, but these are also caused by weathering, which may cause a strong velocity reduction.

The maps shown in Figures 6–8 highlight the extreme geological complexity in the study region. In this research and the previous studies (e.g., [13]), the existence of good lithostratigraphic information is of vital importance to correctly generalize/extend the V_{s30} and soil type data points to the corresponding polygon representing a certain geological formation. In certain areas, where sediment thickness variations to bedrock (where $V_S >$ 800 m/s) depth are present, these lithological data are insufficient to generalize the data points. In the map of Figure 7, we show several points where soil classification is of type E but due to polygon averaging, soil type is labeled as C or even B. This emphasizes the need to have a much larger number of measurements to produce accurate results at a finer scale and define these areas of E soil type with accuracy. The tentative map produced using machine learning (Figure 8) supports this hypothesis.

As stated above, further complexity may be introduced in these maps if the bedrock (Mesozoic and Pre-Mesozoic) outcropping areas, where the weathered layer may be in some places thick, are covered with more Vs measurements. Resonance effects causing the surficial, thick, weathered layer to produce a strong amplification of seismic waves due to the velocity contrast and may cause certain areas to fall into soil type E (see following section). Tables 1, 3 and A1 show us that siliciclastic Pre-Mesozoic, Cretaceous, or Jurassic lithologies may also fall into class B or C.

Though in this work we have a limited number of Vs measurements in bedrock (here in the sense of Mesozoic and Pre-Mesozoic compacted formations) outcrops (6), profile PS45, e.g., acquired over Jurassic weathered sandstones and limestones, presents velocities of 270 m/s and 1080 m/s, respectively, for the first and second layers at a depth of 7 m and its soil class falls into C category. Bedrock areas should therefore be revisited in the future with more measurements, particularly in areas where critical facilities are placed or areas with strong population density.

Unmapped depth/thickness variations in the different geological formations and the lack of information on the distribution of lithological boundaries possibly introduced errors in the V_{s30} map and, hence, in the soil type map.

In the V_{s30} map presented here (Figure 6), Vs classes larger than 60 m/s were used. Assuming a maximum error of 20% in seismic velocities and layer thicknesses, a maximum

error in V_{s30} below up to 60 m/s is estimated. We expect that measurement errors in velocities/depths are well below this 20% estimate, implying that the velocity classes present in the V_{s30} and soil type maps are not affected by V_{s30} errors.

Previously available V_{s30} or soil type maps for Portugal (Figure 9) either have a reduced number of direct shear wave velocity measurements and use a gross geology-based extrapolation [12] or have been built based on proxies and cover the entire country, showing less detail in the study area. Silva et al. (Figure 4 of [11], Figure 9) have produced V_{s30} maps for Portugal using the geological approach of Wills and Clahan [11] and the topographic-slope method of [53]. The latter method may not be adequate for the study area, as the data acquired in the present work show large V_{s30} variations inside the LTV alluvial plains. Also, the maps presented here are more accurate due to the use of direct Vs information, compared to the map by Silva et al. [11], which used proxies and Vs in geological analogs.

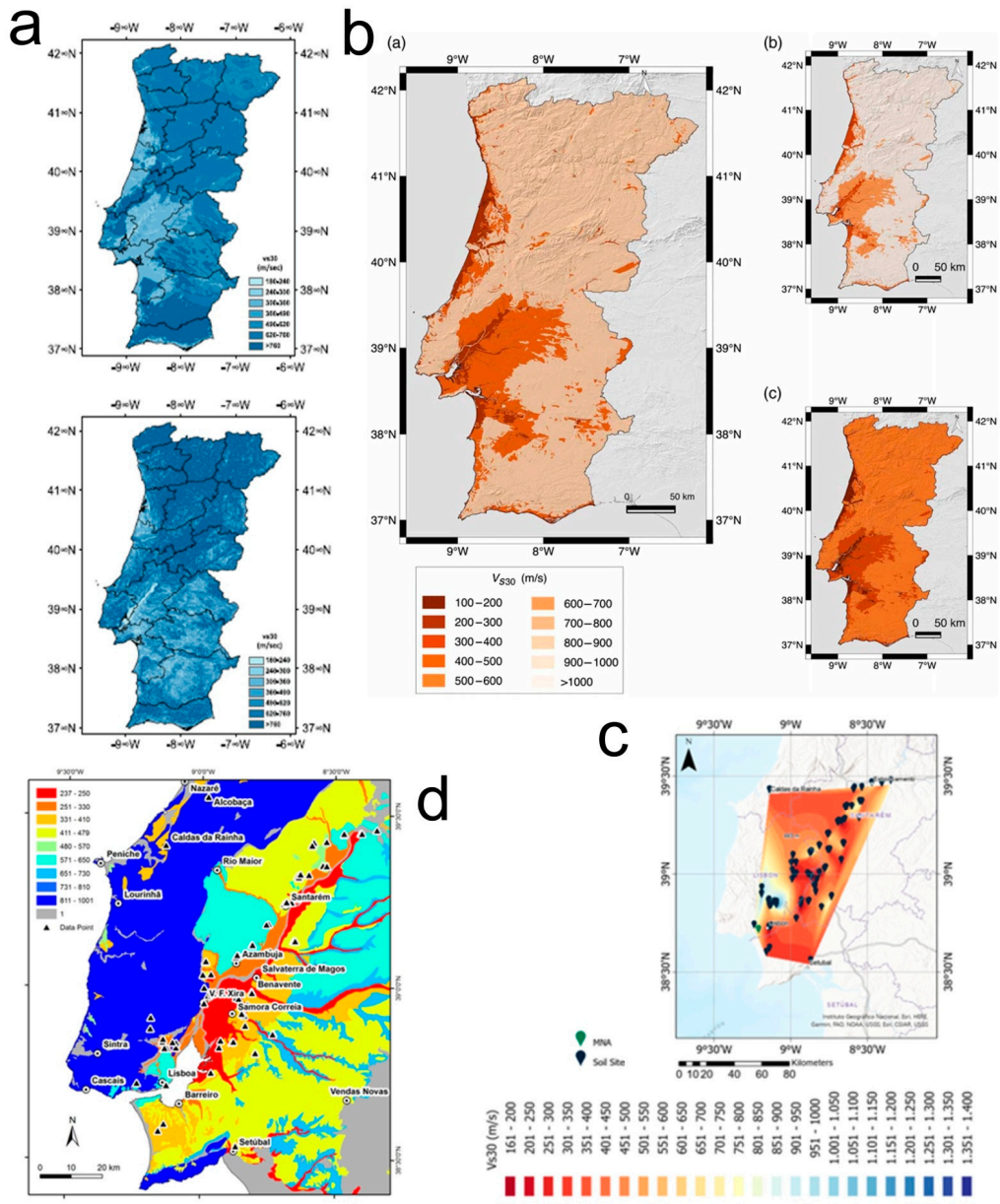

Figure 9. V_{s30} and soil classification maps produced in previous works. (**a**) Silva et al. [11]; (**b**) Vilanova et al. [10]; (**c**) Gögen et al. [66]; (**d**) Carvalho et al. [13].

The V_{s30} maps produced in this work are based on more than twice the data points used by [13] and, without any doubt, are the most detailed maps produced so far in the LTV region. The maps presented here show V_{s30} variations inside several geological polygons belonging to a single V_{s30} class of the map by Silva et al. [11], such as in the Miocene and the Quaternary units. The maps presented by Vilanova et al. [10] are also produced at a national level, but direct Vs measures in the study area are less than 50 and proxies were used to generalize the data points to the geological polygons.

In this work, our generalization of the V_{S30} data points that fell within a particular 1::000,000 scale geological polygon was performed using 1:50,000 geological maps and unpublished geological information at the 1:25,000 scale, and also using RS data with a resolution of 10 m. In spite of this very high spatial resolution data, the maps will always be limited by the number of velocity measurements and the geological complexity of the study area. The latter is expressed in the velocity standard errors obtained for each geological formation (Table 1), which we have previously associated with lithological variations with each geological formation.

Despite the high-spatial resolution of RS data, the maps will always be limited to the coarser dataset, in this case, the 25,000-scale geological/lithological information available, assuming that RS data can properly generalize the V_{S30} datapoints to this scale. The map obtained in Figure 8 using the ML approach and standard deviations shown in Table 1 show us that this is not always the case for all geological formations, but we can expect that our maps will contain information at the 1:25,000 scale, though they will surely contain some accuracy than can only be mitigated with more seismic velocity measurements.

V_{S30} and soil classification maps reflect soil properties that strongly influence observed seismic intensities (e.g., [23,49,51]). As stated in the Introduction section, the lack of macroseismic information in the study area prevents the elaboration of detailed seismic hazard maps based on seismic intensities. Maximum intensity and peak-ground acceleration (PGA) maps for Portugal clearly demonstrate that the study area is more prone to earthquake shaking during moderate to large events (e.g., [11] for PGA and [67] for maximum intensity), either for local or plate boundary seismogenic sources. The study area is also prone to liquefaction effects, as reported historically and several recent studies ([5,67,68]).

The maps presented in this work (Figures 6–8) identify the areas susceptible to liquefaction. The areas where liquefaction has been historically reported have been identified in Figure 6 with stars, and they are sited over C soil classification. Other nearby areas very susceptible to liquefaction, according to the recent studies [67,68], are also of type C soil, demonstrating that V_{S30} and soil class are not good parameters to identify liquefaction prone areas within areas with moderate hazard. For a better assessment of the liquefaction potential, local, in situ studies should be performed [68].

Our tentative map of a finer scale produced using machine learning techniques with random forest classification shows promising results (Figure 8). Alluvium-covered areas are well trained, presenting expected classes of C and D. Other areas covered by Cenozoic sediments are classified with B and C, in agreement with the map of Figure 7, but minor areas are classified with A, which seems unrealistic. Similarly, the training of the algorithm still needs to be improved for the area covered by harder, more compacted Mesozoic rocks, and also for Paleozoic and igneous outcropping regions. These areas receive classifications A, B and C, mostly A and B. Though for the reasons explained above, we could expect classifications of B and C in an area where the weathered layer is thick, we expect the larger part of this region to be of class A. In Figure 10, a trade-off between the two maps, resampled for exclusion of unmapped areas with no data collection of Figure 7, depicts the main differences with a striking exchange for classes A and B. It is worth noticing that the RS images are time-dependent, regarding coverage and land use, and may not necessarily

reflect the complexity and variability of underlying geology as highlighted above. Despite the ML random forest classifier being powerful and effective, it requires finer tuning of the parameters like the number of trees and number of variables [64] and the inclusion of balanced classes to provide more detailed insights and a better comprehension of these exploratory data. Additionally, the RS data compressed to MNF factors processed should also be tested using more variables derived from RS such as mineralogical indices, i.e., ferrous and ferric iron and clays to further support surface geology. Considering the impact on Vs30 velocities of Digital Elevation Models (DEM), slope, and roughness [69], other relevant data should also be exploited for soil map determination. In fact, the 174-point data benefited from the additional information and was already categorized by soil classes.

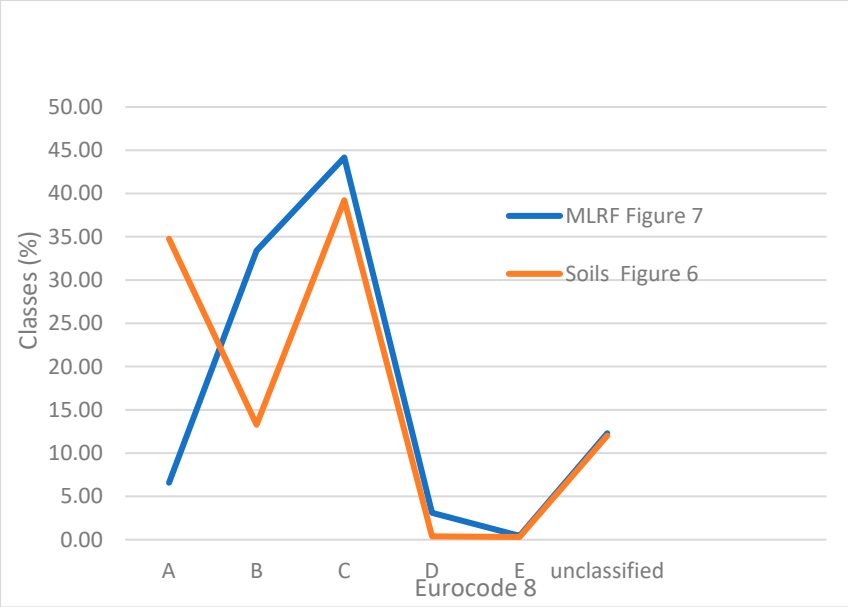

Figure 10. Results of Eurocode 8 classification using methodology by built-up polygons with additional geological information (Figure 7) and using machine learning random forest trained with point field measurements assigned to Eurocode 8 (Figure 8).

Concerning machine learning, other models and approaches, including hybrid models, should be undertaken, and decision and improvements based on fine tuning should be made to increase robustness of the results.

In short, hard-rock areas are being classified as more hazardous than expected, while intermediate areas with expected classes of B and C (where Cenozoic sediments outcrop) have minor areas classified as A. This is probably due to two major reasons: (i) the RS images accurately map the alluvial sediments but are possibly unsuited to map lithological changes; (ii) as we only have 173 shear wave measures in the study area, unable to cover all the existent geological polygons at the 1:1,000,000 scale where the soil classification was determined, and the pixel of RS images is 10 m, the geophysical information is limited when compared to RS data, resulting in an overdetailed mapping of soil classes in Figure 8. While a detailed lithological mapping is not available for the study area to check hypothesis (i), the use of geological mapping at the 1:50,000 scale (also not available for the entire study area) may improve the problem presented by (ii). Further statistical analysis should also take the images into account to understanding the trade-off between geology and land cover.

To summarize, the use of the ML technique to further detail the hazard maps should be better explored in the future, using an additional few tens of shear wave measurements and geological cartography at a finer scale. These two aspects will certainly improve the training of the ML algorithm random forest, or others, and an improvement in the results.

Using direct velocity measurements instead of soil classes may also improve the results. This tentative soil classification using ML methods seems, however, like a good approach for the future, though it may be limited by the need to better understand the relationship between lithology and the factors to which the RS images respond to.

6. Conclusions

The LTV is a highly populated region in central Portugal, with a population of around 3.7 million. It includes the metropolitan area of Lisbon, the capital of the country, and several vital critical facilities and communication networks. The region has been affected in the past by historical earthquakes causing massive destruction and loss of lives, recurring every 150–250 years, approximately. Due to the large recurrence times for large magnitude earthquakes in this region, macroseismic data or earthquake records are scarce. Therefore, performing the characterization of the near-surface soils, sediments and rocks for site effects and microzonation studies using Vs is extremely important.

In the present research, Vs measurements were carried out mostly with seismic refraction profiles and seismic noise data, together with a few cross-hole measurements and data from other bibliographical sources. Together with lithological, geological data gathered from detailed local geological surveys at each Vs site, remote sensing imagery and borehole data, including SPT information, was used to produce V_{s30} and soil classification maps of the LTV region. Though digital vector cartography at the 1:1,000,000 scale was used, the maps presented here contain information at a lower scale once many of the geological polygons were subdivided using lithological and remote sensing data at lower scales.

The results presented here show what has been known for decades: that the study region is highly complex with spatially varying layer thicknesses and sharp lithological changes. Such high complexity prevents a simple geographical generalization/extension of the Vs and soil classification data points to geological formations. A geological-based approach, supported by satellite images and detailed lithological information, was employed to undertake the challenging task of generalizing the calculated data points (seismic velocity and soil types) to the respective geological polygons they pertain to. A machine learning classification random forest was also employed to further detail the soil classifications map, using the soil classification for each geological polygon at the 1:1,000,000 scale, the respective geological polygons and remote sensing data. The results presented here strongly suggest the need to acquire additional velocity data accompanied by careful geological and lithostratigraphic analysis, as several areas, some heavily populated, have a strong to moderate seismic risk and need to be further detailed. These areas include not only those covered by soft soils underlain by hard bedrock (class E), but also other areas that are usually considered low risk such as Mesozoic units, that due to weathering and their soft nature may present a moderate to high risk. Though more detailed V_{s30} and soil classification maps of the LTV region are needed, the results here presented are the most detailed maps available for the study area using direct measurements and are already extremely important, contributing to the improvement of the evaluation of seismic risk and mitigation of earthquake damage in the LTV region, and should be used in land planning, civil protection, and seismic hazard assessment purposes.

The results highlight a region of great susceptibility to earthquake shaking (soil class D), but which is mostly an agricultural area with little human occupation. However, although central Lisbon has a low seismic hazard (class B), the Metropolitan Area of Lisbon is sited in an area of moderate seismic hazard (class C) and some areas even fall into very hazardous soil type class E, namely the areas close to the river Tagus and in the Loures council. A large part of the study area, mostly covered by Pleistocene and Pliocene sediments, and in lesser extent by Miocene deposits, where district capital of Setúbal and several small cities and villages (Barreiro,

Almada, Seixal, Vendas Novas, Salvaterra, Coruche, etc.) (Figure 7) are located, totaling more than 580,000 habitants, has a moderate seismic hazard and risk.

The tentative soil classification map produced with the ML technique shows the potential of the method to further detail the hazard maps, but several measurements are still needed, together with finer scale geological maps and a better understanding of the remote sensing data response to lithological changes. After these steps are taken, the methodology can be employed to produce hazard maps useful for civil protection agencies and municipal land planning without the need of a substantially larger seismic velocity dataset than the one used in this work.

Author Contributions: Conceptualization, J.C. and R.D.; methodology, J.C., R.D., J.B., L.Q. and B.C.; formal analysis, L.Q.; investigation, L.Q.; resources, J.C., R.D., J.B., L.Q. and B.C.; data curation, J.C., R.D., J.B., L.Q. and B.C.; writing—original draft preparation, J.C.; writing—review and editing, R.D., J.B., L.Q. and B.C.; visualization, J.C., R.D., J.B. and L.Q. All authors have read and agreed to the published version of the manuscript.

Funding: This research was funded by Fundação para a Ciência e a Tecnologia, grant numbers PTDC-CTE/GIX/102245/2008, PTDC-CTE/GIX/103032/2008, PBCIC/C/CTA/2107/95 and UIDB/06107, by European Union through the European Regional Development Fund under COMPETE 2020, grant number POCI-01-0145-FEDER-007690, and the APC was funded by University of Évora.

Data Availability Statement: All raw seismic refraction data (SEG-2 files) used acquired in the scope of this work are not available online but can be obtained on request by contacting Laboratório Nacional de Energia e Geologia (www.lneg.pt) or the corresponding author. Digital geological data are owned by LNEG and is commercially available or published under CCBY licensing at https://geoportal.lneg.pt/en/, https://geoportal.lneg.pt/en/productslist/, accessed on 1 April 2025. Borehole reports are commercially available at https://geoportal.lneg.pt/en/databases/tecnibase/#!/?anoQuery=Anteriores%20a&pagina=1&sortOrder=asc, accessed on 1 April 2025 and can be obtained digitally (pdf) on request.

Acknowledgments: Eng.º Bruno Casal/Sondagens Casal and Eng.º Viana da Fonseca/project Liquefact are further acknowledged for allowing the inclusion of refraction data acquired under the scope of services. The authors further acknowledge the field crew that acquired seismic refraction data, consisting of J. Gomes, F. Caneiras and M. Silva. This article contains Modified Copernicus Sentinel data [2020]. This document was improved by the suggestions and comments of three anonymous reviewers.

Conflicts of Interest: The authors declare no conflicts of interest.

Appendix A

Table A1. Layer depths, shear wave velocities, V_{S30}, and soil type for each data point used in this work. V_Si: S-wave velocity for layer i in m/s. Di: depth to layer i in m. Soil: soil class according to Eurocode 8 [15]. X,Y data point coordinates in ETRS89 system, datum WGS84, in meters. Data points starting with PS indicate refraction profiles whose S-wave velocity was extrapolated from P-wave velocity using the approach presented in this article. TVi: data published by [31]. 1: Lisbon downtown north; 2: Lisbon downtown center; 3: Lisbon downtown south.

Profile	Geologycal Formation	Main Lithologies	Age	V_S1	V_S2	V_S3	D2	D3	V_{S30}	Soil	X	Y
TOJ1	Alluvium	clays	Holocene	99	408	-	16	-	153	S1	−87,573	−91,681
VFX5	Alluvium	clays	Holocene	84	222	372	5	12	215	C	−72,915	−76,570
PM12	Alluvium	clays	Holocene	247	322	-	8	-	297	C	−52,723	−62,429
RS15	Alluvium	clays	Holocene	164	276	-	11	-	220	C	−45,872	−46,622
ARR23	Alluvium	clays	Holocene	172	665	-	15	-	274	C	−23,513	−24,320
BEN31	Alluvium	clays	Holocene	150	233	-	14	-	185	C	−58,942	−75,251

Table A1. *Cont.*

Profile	Geologycal Formation	Main Lithologies	Age	V_S1	V_S2	V_S3	D2	D3	V_{S30}	Soil	X	Y
PAN46	Alluvium	clays	Holocene	121	250	-	10	-	186	C	−68,898	−91,074
PSE49	Alluvium	clays	Holocene	96	142	-	10	-	123	S1	−61,123	−83,025
6_7	Alluvium	sands, clays	Holocene	80	505	419	3	-	326	C	−34,953	−30,130
VFX34	Alluvium	clays	Holocene	152	531	-	0.2	-	522	B	−74,170	−79,070
PS34	Alluvium	clays	Holocene	89	267	-	1	-	246	C	−71,842	−75,896
PS40	Alluvium	clays	Holocene	21	431	-	1	-	296	C	−87,566	−91,398
PS22	Alluvium	clays	Holocene	166	276	-	4	-	254	C	−44,125	−45,339
PS32	Alluvium	clays	Holocene	74	162	226	1	3	211	C	−69,367	−93,326
PS25	Alluvium	sands, clays	Holocene	302	442	818	3	27	445	B	−53,758	−62,624
PT_05	Alluvium	sands, clays	Holocene	80	233	504	4	14	245	C	−79,821	−118,132
PS19	Alluvium	clays	Holocene	63	375	-	1	-	301	C	−65,329	−75,895
PS3	Alluvium	clays	Holocene	228	656	-	5	-	488	B	−23,071	−24,450
A10	Alluvium	clays	Holocene	406	617	-	6	-	555	B	−63,918	−64,246
Si1	Alluvium	clays	Holocene	140	210	-	13	55	173	D	−64,434	−76,610
Si5	Alluvium	clays	Holocene	135	220	-	12	31	176	D	−62,348	−72,583
Si6	Alluvium	clays	Holocene	100	150	248	5	42	101	D	−65,540	−72,469
Si7	Alluvium	clays	Holocene	115	145	565	3	24	165	D	−67,566	−78,379
Si9	Alluvium	clays	Holocene	105	260	-	11	55	169	D	−66,206	−82,499
Si11	Alluvium	clays	Holocene	115	160	-	24	48	122	S1	−69,953	−79,690
Si12	Alluvium	clays	Holocene	110	180	-	11	40	146	D	−69,906	−75,944
Si13	Alluvium	clays	Holocene	80	140	-	5	33	124	D	−72,654	−79,170
VFX_SB_2	Alluvium	clays	Holocene	82	98	489	2	20	131	D	−73,397	−78,288
VFX_SB_3	Alluvium	clays	Holocene	80	335	415	5	30	219	C	−72,765	−76,635
VFX_SB_4	Alluvium	clays	Holocene	80	217	463	5	30	169	D	−70,182	−79,264
VFX_SB_5	Alluvium	clays	Holocene	80	251	629	4	30	195	C	−68,939	−791,623
VFX_SB_6	Alluvium	clays	Holocene	80	273	375	3	30	220	C	−65,739	−79,413
4_2	Alluvium	sands, clays	Holocene	80	323	583	3	14	304	CA	−78,767	−87,496
4_3	Alluvium	clays	Holocene	80	274	1336	4	17	285	E	−74,031	−90,301
4_4	Alluvium	sands, clays	Holocene	80	262	865	4	30	196	C	−72,428	−91,397
LSB_CBL_22	Alluvium	sands, clays	Holocene	80	272	412	3	30	219	C	−30,909	−120,810
LSB_CBL_21	Alluvium	sands, clays	Holocene	80	396	454	5	28	240	C	−34,128	−119,881
Cross-232	Alluvium	clays	Holocene	173	195	200	6	22	191	C	−63,788	−77,259
Cross-304	Alluvium	clays	Holocene	181	184	211	11	19	192	C	−63,001	−77,626
SAM12	Alluvium	sands, clays	Holocene	319	444	-	6	-	410	B	−60,128	−79,509
TV1	Alluvium	landfill, silty sand	Holocene	169	202	525	7.5	24	221	C	−87,406	−105,694
TV2	Alluvium	landfill, silty sand	Holocene	167	207	525	3	22	240	C	−87,265	−106,136
TV3	Alluvium	landfill, silty clay	Holocene	172	177	-	7	-	176	D	−87,500	−105,469
LSB_CBL_5	Alluvium	landfill, silty sand	Holocene	80	396	454	5	28	240	C	−83,978	−102,438
LSB_CBL_3	Alluvium	landfill, clay, silty sand	Holocene	81	200	660	3	14	258	C	−89,088	−100,828
5_8	Alluvium	sands, clays	Holocene	81	377	509	5	-	240	C	−57,801	−65,608
5_9	Alluvium	sands, clays	Holocene	80	341	306	4	-	231	C	−55,836	−65,729
6_8	Alluvium	sands, clays	Holocene	80	218	724	5	-	166	D	−32,328	−31,837

Table A1. *Cont.*

Profile	Geologycal Formation	Main Lithologies	Age	V_S1	V_S2	V_S3	D2	D3	V_{S30}	Soil	X	Y
RM_MG_10	Alluvium	sands, clays	Holocene	80	169	464	5.1	30	142	D	−49,022	−51,707
PT_9	Alluvium	clays	Holocene	80	263	445	3	-	209	C	−73,326	−108,966
PT_12	Alluvium	sands, clays	Holocene	80	491	496	4	-	286	C	−66,105	−102,764
PT_23	Alluvium	sands, clays	Holocene	81	233	333	5	-	178	D	−61,117	−72,191
PT_24	Alluvium	sands, clays	Holocene	80	288	577	3	15	288	C	−58,438	−70,956
PT_25	Alluvium	sands, clays	Holocene	80	264	469	6	-	178	D	−56,934	−68,673
PT_28	Alluvium	sands, clays	Holocene	80	225	385	4	-	180	D	−50,191	−62,128
PT_29	Undif. sands and gravels	sands	Holocene	80	314	441	4	-	229	C	−49,244	−59,555
PT_38	Alluvium	sands, clays	Holocene	80	260	298	3	-	210	C	−32,554	−38,687
PT_40	Alluvium	sands, clays	Holocene	81	433	555	4	24	280	C	−29,448	−33,165
PT_41	Alluvium	sands, clays	Holocene	80	282	468	6	22	204	C	−27,293	−31,022
PT_42	Alluvium	sands, clays	Holocene	80	252	670	3	16	266	C	−26,119	−28,057
PT_43	Alluvium	sands, clays	Holocene	81	345	531	4	-	239	C	−25,405	−25,299
PT_44	Alluvium	sands, clays	Holocene	82	531	519	5	-	278	C	−23,842	−24,283
PENE01	Porto do Concelho Fm.	sands, clays	Holocene	150	400	800	2	5	576	B	−88,815	−123,416
PS29	Eolic sands	sands	Pleistocene	388	550	569	3	8	540	B	−61,969	−82,427
PS17	Undif. sands and gravels	sands, gravel	Pleistocene	70	166	501	0.4	4	371	B	−44,691	−59,035
PS14	Undif. sands and gravels	sands, gravel	Pleistocene	98	230	864	2	8	429	E	−36,167	−44,710
VFX_SB_7	Undifferentiated aeolian sands	sands	Pleistocene	80	226	884	3	-	191	C	−62,313	−80,931
5_11	Undif. Sands	sands	Pleistocene	80	599	386	3	-	354	C	−50,602	−68,011
PT_14	Undifferentiated aeolian sands	sands	Pleistocene	81	519	260	4	-	315	C	−65,068	−96,826
PS20	Undif. sands and gravels	sands, gravel	Pleistocene	162	361	965	2	6	621	E	−55,133	−72,574
PV47	Fluvial terrace deposits	sands	Pleistocene	317	356	-	28	-	318	C	−65,161	−91,764
BEN3	Fluvial terrace deposits	Landfild, sands, gravel	Pleistocene	299	467	-	11	-	384	B	−58,679	−75,796
PS39	Fluvial terrace deposits	sands, gravel	Pleistocene	244	348	564	17	7	489	B	−87,406	−90,523
PS31	Fluvial terrace deposits	sands, gravel	Pleistocene	267	401	465	1	9	436	B	−64,675	−91,464
PS30	Undif. sands and gravel	sands, gravel	Pleistocene	278	376	441	1	11	413	C	−60,893	−86,278
FBE37	Undif. sands and gravel	sands, gravel	Pleistocene	139	406	861	1	5	636	E	−45,209	−58,990
SAM41	Undif. sands and gravels	sands, gravel	Pleistocene	146	246	-	15	-	184	C	−55,851	−73,324
TOJ2	Fluvial terrace deposits	clay sandstones, gravel	Pleistocene	350	513	-	9	-	447	B	−87,613	−90,940
ONO6	Fluvial terrace deposits	sandstones	Pleistocene	225	284	543	17	36	247	C	−71,893	−69,745
PO18	Fluvial terrace deposits	sands, gravel	Pleistocene	211	443	-	5	-	379	B	−35,691	−34,794
BO20	Fluvial terrace deposits	sands, gravel	Pleistocene	264	932	1516	3	22	836	A	−34,478	−27,086

Table A1. *Cont.*

Profile	Geologycal Formation	Main Lithologies	Age	V_S1	V_S2	V_S3	D2	D3	V_{S30}	Soil	X	Y
EN21	Fluvial terrace deposits	gravel, sands	Pleistocene	385	1157	-	19	-	515	B	−29,006	−24,684
STE44	Undif. sands and gravels	sands, gravel	Pleistocene	509	643	-	20	-	549	B	−51,845	−88,816
BEL33	Porto Concelho Fm.	sands, marls	Pleistocene	284	372	-	8	-	344	C	−87,292	−117,867
PT_33	Undif. sands and gravel	sands, gravels	Pleistocene	80	288	350	5	-	200	C	−42,256	−50,274
PT_36	Undif. sands and gravel	sands, gravels	Pleistocene	80	225	466	3	16	235	C	−36,952	−42,628
FONT01	Marco Furado Fm.	sands, gravels	Pleistocene	292	524	-	3		485	B	−82,966	−124,152
4_5	Undifferentiated aeolian sands	sands	Pleistocene	82	452	482	3	-	312	C	−68,075	−92,204
4_15	Undifferentiated aeolian sands	sands	Pleistocene	83	675	478	3.5	30	368	B	−37,762	−104,256
RM_MG_15	Undif. sands	sands	Pleistocene	80	374	360	3.3	-	266	C	−35,100	−57,322
PS18	Undif. sands and gravels	sands, gravel	Pleistocene	319	266	-	1	-	267	B	−46,255	−68,424
PS10	Fluvial terrace deposits	sands, gravel	Pleistocene	178	204	553	0.4	7	397	B	−34,445	−34,863
PS4	Fluvial terrace deposits	gravel, sands	Pleistocene	414	659	-	2	-	630	A	−28,843	−24,437
CHO17	Fluvial terrace deposits	sandstones, gravel	Pleistocene	693	833	-	28	-	700	B	−40,170	−37,676
6_22	Fluvial terrace deposits	gravel, sands	Pleistocene	83	290	489	4	17	258	C	67,55	−49,705
CRA27	Barracão Group	sandstones, gravel	Pliocene	277	391	-	8	-	350	C	−86,365	−27,981
PERU01	Santa Marta Fm.	sandstones, gravel, clays	Pliocene	309	584	-	21		360	C	−81,225	−126,318
PT_6	Santa Marta Fm.	sandstones, gravels, clays	Pliocene	81	291	475	3	20	249	C	−79,935	−115,079
ACT13	Santa Marta Fm.	sandstones, gravels, clays	Pliocene	398	402	-	5	-	401	B	−72,031	−101,451
VER2	Santa Marta Fm.	sandstones, gravels, clays	Pliocene	103	366	502	1	41	338	C	−89,145	−120,125
SET14	Santa Marta Fm.	sandstones, gravels, clays	Pliocene	219	350	-	9	-	298	C	−64,059	−125,143
PS33	Santa Marta Fm.	sandstones, gravels, clays	Pliocene	138	493	797	1	9	608	B	−57,642	−95,147
VFX_SB_24	Ulme Fm.	sandstones, gravel	Pliocene	81	160	667	5	27	147	D	−22,381	−93,612
VFX_SB_25	Ulme Fm.	sandstones, gravel	Pliocene	80	237	445	3	15	246	C	−20,430	−94,611
LSB_CBL_23	Ulme Fm.	sandstones, gravel	Pliocene	80	276	434	3	18	251	C	−28,732	−122,111
6_10	Ulme Fm.	sandstones, gravel	Pliocene	80	338	407	3	30	254	C	−26,788	−35,416
6_11	Ulme Fm.	sandstones, gravel	Pliocene	81	307	511	5	23	231	C	−23,897	−35,894
6_14	Ulme Fm.	sandstones, gravel	Pliocene	80	237	304	3	30	195	C	−15,420	−40,177
6_15	Ulme Fm.	sandstones, gravel	Pliocene	91	245	265	3	30	207	C	−12,837	−41,351

Table A1. *Cont.*

Profile	Geologycal Formation	Main Lithologies	Age	V_S1	V_S2	V_S3	D2	D3	V_{S30}	Soil	X	Y
6_16	Ulme Fm.	sandstones, gravel	Pliocene	111	223	242	4	30	195	C	−9989	−42,589
6_17	Ulme Fm.	sandstones, gravel	Pliocene	80	264	343	3	30	215	C	−7333	−43,906
6_18	Ulme Fm.	sandstones, gravel	Pliocene	84	241	277	4	30	198	C	−4734	−45,447
RM_MG_21	Ulme Fm.	sandstones, gravel	Pliocene	80	252	419	4	-	196	C	−18,271	−63,866
PS24	Ulme Fm	sandstones	Pliocene	103	371	624	0.5	4	538	A	−53,933	−53,686
AZ10	Ulme Fm.	sandstones, gravel	Pliocene	269	492	-	12	-	372	B	−63,918	−64,246
CCP11	Ulme Fm.	sandstones	Pliocene	421	944	-	17	-	557	B	−58,681	−60,173
VCO13	Ulme Fm.	sandstones	Pliocene	459	671	-	1	-	661	B	−53,262	−53,547
PS26	Ulme Fm	sandstones	Pliocene	184	509	944	0.4	26	528	B	−58,464	−60,278
RM_MG_14	Ulme Fm.	sandstones, gravel	Pliocene	81	202	594	2.8	-	177	D	−37,931	−55,910
APL4	Calcários da Musgueira Fm.	sandstones, limestones	Miocene	445	846	-	2	-	791	B	−86,163	−93,577
PS41	Calcários de Entrecampos Fm.	sandstones, limestones, gravel	Miocene	259	513	774	1	8	658	B	−86,941	−93,505
APL3	Calcários de Entrecampos Fm.	sandstones, limestones, gravel	Miocene	227	580	717	3	48	509	B	−87,204	−93,565
PS49	Calcários de Marvila Fm.	sandstones, limestones	Miocene	681	1649	-	3	-	1437	E	−83,186	−91,803
PS48	Areolas de Braço de Prata Fm.	sandstones, limestones	Miocene	238	410	1048	2	6	735	E	−83,259	−93,345
PS47	Areias de Vale de Chelas Fm.	sandstones, limestones	Miocene	180	388	1292	1	5	831	B	−84,333	−91,644
LSB_CBL_4	Areias com Placuna miocenica	sandstones	Miocene	81	402	447	3	30	288	C	−86,175	−101,517
SCPC02	Areias com Placuna miocenica	sandstones	Miocene	115	275	450	3	16	287	C	−94,372	−109,796
SVF30	Areias com Placuna miocenica	sandstones	Miocene	316	524	713	6	43	336	C	−86,436	−105,429
SCPC03	Areias da Quinta do Bacalhau	sandstones	Miocene	140	270	515	3	9	355	C	−94,655	−109,987
BANT02	Areias da Quinta do Bacalhau	sandstones	Miocene	155	565	-	6	47	370	C	−92,813	−109,544
BANT01	Argilas do Forno do Tijolo	clayey sandstones	Miocene	195	1090	-	4	50	676	B	−93,230	−109,533
SCPC01	Argilas do Forno do Tijolo	Clayey, sandstones	Miocene	155	220	800	5	15	311	E	−94,551	−109,919
BANT03	Argilas do Forno do Tijolo	clayey sandstones	Miocene	146	407	1300	2	8	661	B	−93,083	−109,573

Table A1. *Cont.*

Profile	Geologycal Formation	Main Lithologies	Age	V_S1	V_S2	V_S3	D2	D3	V_{S30}	Soil	X	Y
PS7	Tomar Clays Fm.	claystones, sandstones w/carbonate crusts	Miocene	158	349	398	1	5	370	B	−391,648	−28,212
ALC19	Tomar Clays Fm.	claystones, sandstones w/carbonate crusts	Miocene	240	355	561	5	29	335	C	−38,615	−27,319
VFX_SB_18	Undif. Alcoentre Fm. and Tomar Clays	claystones, sandstones w/carbonate crusts	Miocene	80	364	485	5	30	229	C	−35,352	−88,319
VFX_SB_20	Undif. Alcoentre Fm. and Tomar Clays	claystones, sandstones w/carbonate crusts	Miocene	82	297	488	3	30	235	C	−32,409	−89,880
6_20	Undif. Alcoentre Fm. and Tomar Clays	claystones, sandstones	Miocene	80	263	440	4	23	221	C	1116	−48,081
RM_MG_17	Undif. Alcoentre Fm. and Tomar Clays	claystones, sandstones	Miocene	80	318	407	3.3	-	240	C	−28,857	−59,827
PS21	Undif. Alcoentre Fm. and Tomar Clays	claystones, sandstones w/carbonate crusts	Miocene	338	778	1227	2	10	905	B	−52,007	−89,089
PS9	Undif. Alcoentre Fm. and Tomar Clays	claystones, sandstones wcarbonate crusts	Miocene	249	821	-	2	-	689	B	−43,486	−38,493
PS8	Undif. Alcoentre Fm. and Tomar Clays	claystones, sandstones wcarbonate crusts	Miocene	178	456	-	3	-	402	B	−42,967	−37,537
6_4	Undif. Alcoentre Fm. and Tomar Clays	claystones, sandstones	Miocene	233	1349	982	4	30	291	C	−43,183	−26,549
6_5	Undif. Alcoentre Fm. and Tomar Clays	claystones, sandstones wcarbonate crusts	Miocene	80	218	724	5	30	166	D	−40,539	−27,905
6_6	Undif. Alcoentre Fm. and Tomar Clays	claystones, sandstones wcarbonate crusts	Miocene	80	381	464	3	30	274	C	−37,946	−29,245
RM_MG_5	Undif. Alcoentre Fm. and Tomar Clays	sandstones, claystones wcarbonate crusts	Miocene	80	396	454	5	28	248	C	−63,217	−46,231
4_19	Undif. Alcoentre Fm. and Tomar Clays	claystones, sandstones wcarbonate crusts	Miocene	80	467	739	3	21	339	C	−25,872	−108,768
VF16	Undif. Alcoentre Fm. and Tomar Clays	sandstones, claystones wcarbonate crusts	Miocene	171	406	697	2	22	415	B	−43,886	−38,062

Table A1. *Cont.*

Profile	Geologycal Formation	Main Lithologies	Age	V_S1	V_S2	V_S3	D2	D3	V_{S30}	Soil	X	Y
SAN26	Alcoentre Fm.	sandstones, claystones	Miocene	284	449	-	7	-	392	B	−48,236	−46,973
CAR7	Alcoentre Fm.	sandstones, claystones wcarbonate crusts	Miocene	261	405	805	2	24	429	B	−74,515	−69,918
CHE8	Alcoentre Fm.	sandstones, claystones	Miocene	236	305	-	6	-	289	C	−73,562	−65,709
AZ9	Alcoentre Fm.	claystones, sandstones	Miocene	400	574	-	6	-	526	B	−62,989	−63,604
5_6	Alcoentre Fm.	sandstones, claystones wcarbonate crusts	Miocene	80	274	404	3	30	215	C	−64,276	−62,414
SAN14	Alcoentre Fm.	sandstones, claystones wcarbonate crusts	Miocene	148	318	512	1	38	303	C	−47,361	−46,486
PS28	Alcoentre Fm.	sanstones, claystones	Miocene	265	296	480	2	7	417	A	−73,533	−65,477
PS27	Alcoentre Fm.	claystones, sanstones wcarbonate crusts	Miocene	291	1069	-	2	-	921	C	−63,425	−63,513
PS23	Alcoentre Fm.	sandstones, claystones wcarbonate crusts	Miocene	250	283	-	1	-	282	B	−47,482	−46,502
PS42	Alcoentre Fm.	sandstones, claystones wcarbonate crusts	Miocene	136	332	654	1	9	477	A	−74,520	−69,856
RM_MG_3	Alcoentre Fm.	sandstones, claystones wcarbonate crusts	Miocene	80	227	479	3	14	251	C	−68,930	−43,533
RM_MG_4	Alcoentre Fm.	sandstones, claystones wcarbonate crusts	Miocene	80	206	589	4	12	251	C	−65,687	−44,872
LSB_CBL_2	Benfica Fm.	claystones, sandstones, gravels, wcarbonate crusts	Paleogene	80	526	575	4	30	302	C	−91,942	−99,496
4_1	Benfica Fm.	claystones, sandstones, gravels, wcarbonate crusts	Paleogene	80	221	546	3	12	264	C	−81,198	−87,523
5_26	Vale do Guizo Fm.	claystones, sandstones, gravels, wcarbonate crusts	Paleogene	80	221	408	4	29	184	C	−6031	−85,302
4_20	Vale do Guizo Fm.	claystones, sandstones, gravels, wcarbonate crusts	Paleogene	80	365	550	3	30	267	C	−23,226	−109,786

Table A1. *Cont.*

Profile	Geologycal Formation	Main Lithologies	Age	V_S1	V_S2	V_S3	D2	D3	V_{S30}	Soil	X	Y
5_2	Monsanto Fm.	claystones, sandstones, gravels, wcarbonate crusts	Paleogene	80	286	474	3	30	230	C	−75,444	−57,829
CNX29	Volcanic Complex of Lisbon	weathered basalt	Cretaceous	186	500	2096	2	10	781	B	−95,943	−104,700
PS35	Volcanic Complex of Lisbon	weathered basalt	Cretaceous	167	620	1894	1	8	1039	A	−91,538	−87,173
LSB_CBL_1	Volcanic Complex of Lisbon	weathered basalt	Cretaceous	80	448	385	3	30	307	C	−94,921	−98,374
RM_MG_1	Almargem Fm.	sandstones, mudstones	Cretaceous	80	268	335	3	25	221	C	−74,345	−41,317
PS45	Serreira Fm.	sandstones, clastones	Cretaceous	271	1077	-	1	-	998	A	−91,372	−83,622
PS43	Abadia	claystones, sandstones	Upper Jurassic	164	536	-	7	-	345	C	−74,113	−74,071
PS1	Gneisso-migmatitic Fm.	gneisses	Pre-Cambrian	75	1240	-	1	-	720	B	−72,608	−12,220

References

1. Justo, J.L.; Salwa, C. The 1531 Lisbon earthquake. *Bull. Seismol. Soc. Am.* **1998**, *88*, 319–328. [CrossRef]
2. Grandin, R.; Borges, J.F.; Bezzeghoud, M.; Caldeira, B.; Carrilho, F. Simulations of strong ground motion in SW Iberia for the 1969 February 28 (MS = 8.0) and the 1755 November 1 (M* 8.5) earthquakes–II. Strong ground motion simulations. *Geophys. J. Int.* **2007**, *171*, 807–822. [CrossRef]
3. Besana-Ostman, G.M.; Vilanova, S.P.; Nemser, E.S.; Falcão-Flor, A.; Heleno, S.; Ferreira, H.; Fonseca, J.D. Large Holocene Earthquakes in the Lower Tagus Valley Fault Zone, Central Portugal. *Seismol. Res. Lett.* **2012**, *83*, 67–76. [CrossRef]
4. Gutscher, M.A.; Dominguez, S.; Westbrook, G.K.; Le Roy, P.; Rosas, F.; Duarte, J.C.; Terrinha, P.; Miranda, J.M.; Graindorge, D.; Gailler, A.; et al. The Gibraltar subduction: A decade of new geophysical data. *Tectonophysics* **2012**, *574–575*, 72–91. [CrossRef]
5. Cabral, J.; Moniz, C.; Batló, J.; Figueiredo, P.; Carvalho, J.; Matias, L.; Teves-Costa, P.; Dias, R.; Simão, N. The 1909 Benavente (Portugal) earthquake: Search for the source. *Nat. Hazards* **2013**, *69*, 1211–1227. [CrossRef]
6. Baptista, M.A.; Miranda, J.M. Evaluation of the 1755 Earthquake source Using Tsunami Modeling. In *The 1755 Lisbon Earthquake: Revisited*; Mendes Victor, L., Sousa Oliveira, C., Azevedo, J., Ribeiro, A., Eds.; Springer: New York, NY, USA, 2009; Volume 1, pp. 425–432.
7. Buforn, E.; Udías, A.; Colombás, M.A. Seismicity source mechanisms and tectonics of the Azores-Gibraltar plate boundary. *Tectonophysics* **1988**, *152*, 89–118. [CrossRef]
8. Carvalho, J.; Cabral, J.; Gonçalves, R.; Torres, L.; Mendes-Victor, L. Geophysical Methods Applied to Fault Characterization and Earthquake Potential Assessment in the Lower Tagus Valley, Portugal. *Tectonophysics* **2006**, *418*, 277–297.
9. Vilanova, S.P.; Nemser, E.; Besana-Ostman, G.M.; Bezzeghoud, M.; Borges, J.F.; Brum da Silveira, A.; Cabral, J.; Carvalho, J.; Cunha, P.P.; Dias, R.P.; et al. Incorporating Descriptive Metadata into Seismic Source Zone Models for Seismic Hazard Assessment: A case study of the Azores-West Iberian region. *Bull. Seismol. Soc. Am.* **2014**, *104*, 1212–1229. [CrossRef]
10. Vilanova, S.P.; Narciso, J.; Carvalho, J.P.; Lopes, I.; Quinta-Ferreira, M.; Pinto, C.C.; Moura, R.; Borges, J.; Nemser, E.S. Developing a Geologically Based VS30 Site-Condition Model for Portugal: Methodology and Assessment of the Performance of Proxies. *Bull. Seismol. Soc. Am.* **2018**, *108*, 322–337. [CrossRef]
11. Silva, V.; Crowley, H.; Varum, H.; Pinho, R. Seismic risk assessment for mainland Portugal. *Bulletin of Earthquake Engineering* **2015**, *13*, 429–457. [CrossRef]
12. Teves-Costa, P.; Rodrigues, I.; Torres, R.J.G.; Carvalho, J.; Almeida, I.M.; Borges, J.F. Vs30 estimation using ambient vibrations and seismic refraction experiments–Application to the Lower Tagus Valley (Portugal). In Proceedings of the Joint Assembly IAHS-IAPSO-IAPSEI, Gotemburg, Sweden, 22–26 July 2013.

13. Carvalho, J.; Dias, R.; Ghose, R.; Borges, J.; Narciso, J.; Pinto, C.; Leote, J. Near surface characterization of the Lisbon and Lower Tagus Valley Area, Portugal for seismic hazard assessment: VS30 and soil classification maps. *Bull. Seismol. Soc. Am.* **2018**, *108*, 2854–2876. [CrossRef]
14. *EN 1998-1*; CEN Eurocode 8—Design of Structures for Earthquake Resistance. Part 1: General Rules, Seismic Actions and Rules for Buildings. European Committee for Standardization: Brussels, Belgium, 2004.
15. Borcherdt, R.D. Estimates of site-dependent response spectra for design (methodology and justification). *Earth. Spectra* **1994**, *10*, 617–653. [CrossRef]
16. Penelis, G.G. Eurocode 8: Characterization of Seismic Action, Design Spectra, Future Trends. In Proceedings of the SERINA-Seismic Risk: An Integrated Seismological, Geotechnical and Structural Approach, Thessaloniki, Greece, 21–27 September 1997; pp. 479–492.
17. Pitilakis, K.; Riga, E.; Anastasiadis, A. Design spectra and amplification factors for Eurocode 8. *Bull. Earthq. Eng.* **2012**, *10*, 1377–1400. [CrossRef]
18. Pitilakis, K.; Riga, E.; Anastasiadis, A. New Design spectra in Eurocode 8 and Preliminary Application to the Seismic Risk of Thessaloniki, Greece. In *Perspectives on Earthquake Geotechnical Engineering. Geotechnical, Geological and Earthquake Engineering*; Ansal, A., Sakr, M., Eds.; Springer: Cham, Switzerland, 2015; Volume 37, pp. 45–91. [CrossRef]
19. Gouveia, F.; Viana da Fonseca, A.; Carrilho Gomes, R.; Teves-Costa, P. Deeper Vs profile constraining the dispersion curve with the ellipticity curve: A case study in Lower Tagus Valley, Portugal. *Soil Dyn. Earthq. Eng.* **2018**, *109*, 188–198. [CrossRef]
20. Borges, J.F.; Bezzeghoud, M.; Caldeira, B.; Carvalho, J. Ground-motion simulation in the Lower Tagus Valley Basin. *Pure Appl. Geophys.* **2015**, *172*, 2411–2420. [CrossRef]
21. Borges, J.F.; Silva, H.G.; Torres, R.J.G.; Caldeira, B.; Bezzeghoud, M.; Furtado, J.A.; Carvalho, J. Inversion of ambient seismic noise HVSR to evaluate velocity and structural models of the Lower Tagus Basin, Portugal. *J. Seismol.* **2015**, *20*, 875–887. [CrossRef]
22. Kanlı, A.I.; Tildy, P.; Prónay, Z.; Pınar, A.; Hermann, L. Vs30 mapping and soil classification for seismic site effect evaluation in Dinar region, SW Turkey. *Geophys. J. Int.* **2006**, *165*, 223–235. [CrossRef]
23. Sucuoğlu, H.; Akkar, S. *Basic Earthquake Engineering: From Seismology to Analysis and Design*; Springer: Cham, Switzerland, 2014. [CrossRef]
24. Ghose, R.; Goudswaard, J. Integrating S-wave seismic reflection data and 239 cone-penetration-test data using a multiangle multiscale approach. *Geophysics* **2004**, *69*, 440–459. [CrossRef]
25. Ghose, R. A microelectromechanical system digital 3C array seismic cone penetrometer. *Geophysics* **2012**, *77*, WA99–WA107. [CrossRef]
26. Zhubayev, A.; Ghose, R. Contrasting behavior between dispersive seismic velocity and attenuation: Advantages in subsoil characterization. *J. Acoust. Soc. Am.* **2012**, *131*, EL170–EL176. [CrossRef]
27. Palmer, D. An introduction to the generalized reciprocal method of seismic refraction interpretation. *Geophysics* **1981**, *46*, 1508–1518. [CrossRef]
28. Dobrin, M.B.; Savitt, C.H. *Introduction to Geophysical Prospecting*; McGraw-Hill: New York, NY, USA, 1989; pp. 1–890.
29. Palmer, D.; Shadlow, J. Integrating long and short wavelength statics with the generalized reciprocal method and the refraction convolution section. *Explor. Geophys.* **2008**, *39*, 139–147. [CrossRef]
30. Teves-Costa, P.; Almeida, I.M.; Rodrigues, I.; Matildes, R.; Pinto, C. Geotechnical characterization and seismic response of shallow geological formations in downtown Lisbon. *Ann. Geophys.* **2014**, *57*, S0436.
31. Nakamura, Y. A Method for Dynamic Characteristics Estimation of Subsurface using Microtremor on the Ground Surface. *Q. Rep. Railw. Tech. Res. Inst. (RTRI)* **1989**, *30*, 25–33.
32. LNEG. *Geological Map of Portugal Scale 1: 1 000 000*; Laboratório Nacional de Energia e Geologia: Alfragide, Portugal, 2010.
33. Carvalho, J.; Pinto, C.; Rabeh, T.; Dias, R.; Torres, L.; Borges, J.; Torres, R.; Duarte, H. Tectonic Evolution of an Intraplate Basin: The Lower Tagus Cenozoic Basin, Portugal. *Basin Res.* **2017**, *9*, 636–657. [CrossRef]
34. Pais, J.; Cunha, P.P.; Pereira, D.; Legoinha, P.; Dias, R.; Moura, D.; Silveira, A.B.; Kullberg, J.C.; González-Delgado, J.A. *The Paleogene and Neogene of Western Iberia (Portugal): A Cenozoic Record in the European Atlantic Domain*, 1st ed.; Springer: Cham, Switzerland, 2012; pp. 1–156.
35. Moony, H.H. *Handbook of Engineering Geophysics, 1: Seismic*; Bison Instruments, Inc.: Chanhassen, MN, USA, 1980.
36. Rafek, A.-G. Depth of penetration of geophysical exploration methods as applied in shallow geological engineering investigations. *Bull. Seismol. Soc. Malays.* **1989**, *23*, 21–28. [CrossRef]
37. Rucker, M.L. Applying the Seismic Refraction Technique to Exploration for Transportation Facilities. In *Geophysics 2000, Proceedings of the First International Conference on the Application of Geophysical Methodologies to Transportation Facilities and Infrastructure, St. Louis, MO, USA, 11–15 December 2000*; AMEC Earth & Environmental, Inc.: Phoenix, AZ, USA, 2000; pp. 1–3.
38. Hunt, R.E. *Geotechnical Investigation Methods: A Field Guide for Geotechnical Engineers*; CRC Press (Taylor & Francis Group): Boca Raton, FL, USA, 2006.

39. Knödel, K.; Lange, G.; Voigt, H.J. *Environmental Geology: Handbook of Field Methods and Case Studies*; Springer: Berlin, Germany, 2007.
40. Maunde, A.; Bassey, N.E. Seismic Refraction Investigation of Fracture Zones and Bedrock Configuration for Geohydrologic and Geotechnical Studies in part of Nigeria's Capital City, Abuja. *J. Earth Sci. Geotech. Eng.* **2017**, *7*, 91–102.
41. Herak, M. ModelHVSR—A Matlab® tool to model horizontal-to-vertical spectral ratio of ambient noise. *Comput. Geosci.* **2008**, *34*, 1514–1526. [CrossRef]
42. Gardner, G.H.F.; Gardner, L.W.; Gregory, A.R. Formation velocity and density—The diagnostic basic for stratigraphic trap. *Geophysics* **1974**, *39*, 770–780. [CrossRef]
43. Brocher, T.M. Empirical Relations between Elastic Wavespeeds and Density in the Earth's Crust. *Bull. Seismol. Soc. Am.* **2005**, *95*, 2081–2092. [CrossRef]
44. Essien, U.E.; Akankpo, A.O.; Igboekwe, M.U. Poisson's Ratio of Surface Soils and Shallow Sediments Determined from Seismic Compressional and Shear Wave Velocities. *Int. J. Geosci.* **2014**, *5*, 1540–1546. [CrossRef]
45. Uyanik, O. Compressional and shear-wave velocity measurements in unconsolidated top-soil and comparison of the results. *Int. J. Phys. Sci.* **2010**, *5*, 1034–1039.
46. Salem, H.S. The compressional to shear-wave velocity ratio for surface soils and shallow sediments. *Eur. J. Environ. Eng. Geophys.* **2000**, *5*, 3–14.
47. Lankston, R.W. The seismic refraction method: A viable tool for mapping shallow targets into the 1990s. *Geophysics* **1990**, *54*, 1535–1542. [CrossRef]
48. Fumal, T.E.; Tinsley, J.C. Mapping shear wave velocities of near-surface geological materials. In *Predicting Aerial Limits of Earthquake Induced Landsliding; In Evaluation of Earthquake Hazards in the Los Angeles Region—An Earth Science Perspective*; US Geological Survey Paper 1360; Ziony, J.I., Ed.; USGS: Reston, WV, USA, 1985; pp. 127–150.
49. Kalkan, E.; Wills, C.J.; Branum, D.M. Seismic Hazard Mapping of California Considering Site Effects. *Earth. Spectra* **2010**, *26*, 1039–1055. [CrossRef]
50. Motazedian, D.; Hunter, J.A.; Pugin, A.; Crow, H. Development of a Vs30 (NEHRP) map for the city of Ottawa, Ontario, Canada. *Can. Geotech. J.* **2011**, *48*, 458–472. [CrossRef]
51. Wills, C.J.; Gutierrez, C.I.; Perez, F.G.; Branum, D.M. A Next Generation Vs30 Map for California Based on Geology and Topography. *Bull. Seismol. Soc. Am.* **2015**, *105*, 3083–3091. [CrossRef]
52. Wills, C.; Petersen, M.; Bryant, W.; Reichle, M.; Saucedo, G.; Tan, S.; Taylor, G.; Treiman, J.A. Site-conditions map for California based on geology and shear-wave velocity. *Bull. Seismol. Soc. Am.* **2000**, *90*, S187–S208. [CrossRef]
53. Wald, D.J.; Allen, T.I. Topographic Slope as a Proxy for Seismic Site Conditions and Amplification. *Bull. Seismol. Soc. Am.* **2007**, *97*, 1379–1395. [CrossRef]
54. Gupta, R.; Tiwari, R.; Saini, V.; Srivastava, N. A Simplified Approach for Interpreting Principal Component Images. *Adv. Remote Sens.* **2013**, *2*, 111–119. [CrossRef]
55. Green, A.A.; Berman, M.; Switzer, P.; Craig, M.D. A transformation for ordering multispectral data in terms of image quality with implications for noise removal. *IEEE Trans. Geosci. Remote Sens.* **1988**, *26*, 65–74. [CrossRef]
56. Teves-Costa, P.; Batlló, J. The 23 April 1909 Benavente earthquake (Portugal): Macroseismic field revision. *J. Seismol.* **2011**, *15*, 59–70. [CrossRef]
57. Cabral, J.; Ribeiro, P.; Figueiredo, P.; Pimentel, N.; Martins, A. The Azambuja fault: An active structure located in an intraplate basin with significant seismicity (Lower Tagus Valley, Portugal). *J. Seismol.* **2004**, *8*, 347–362. [CrossRef]
58. Mendes-Victor, L.A.; Oliveira, C.S.; Azevedo, J.; Ribeiro, A. (Eds.) *The 1755 Lisbon Earthquake: Revisited*; Springer: Cham, Switzerland, 2009.
59. Mendes-Victor, L.A.; Oliveira, C.S.; Pais, I.; Teves-Costa, P. Earthquake Damage Scenarios in Lisbon for Disaster Preparedness. In *Issues in Urban Risk*; NATO ASI Series, 271; Tucker, B.E., Erdik, M., Hwang, C.N., Eds.; Springer: Cham, Switzerland, 1994; pp. 265–289.
60. Johnston, A.C.; Kanter, L.R. Earthquakes in stable continental crust. *Sci. Am.* **1990**, *262*, 68–75. [CrossRef]
61. Perrin, N.D.; Heron, D.; Kaiser, A.; Van Houtte, C. VS 30 and NZS 1170.5 site class maps of New Zealand. In Proceedings of the NZSEE Conference, Rotorua, New Zealand, 10–12 April 2015. Paper 0-07.
62. Matsuoka, M.; Wakamatsu, K.; Fujimoto, K.; Saburoh, M. Average Shear-wave Velocity Mapping Using Japan Engineering Geomorphologic Classification Map. *J. Struct. Mech. Earthq. Eng.* **2005**, *794*, 239–251. [CrossRef]
63. Wills, C.J.; Clahan, K.B. Developing a map of geologically defined site-condition categories for California. *Bull. Seismol. Soc. Am.* **2006**, *96*, 1483–1501. [CrossRef]
64. Belgiu, M.; Drăgu¸t, L. Random forest in remote sensing: A review of applications and future directions. *ISPRS J. Photogramm. Remote Sens.* **2016**, *114*, 24–31. [CrossRef]
65. Adugna, T.; Xu, W.; Fan, J. Comparison of Random Forest and Support Vector Machine Classifiers for Regional Land Cover Mapping Using Coarse Resolution FY-3C Images. *Remote Sens.* **2022**, *14*, 574. [CrossRef]

66. Gögen, B.; Karimzadeh, S.; Lourenço, P.B. Probabilistic Seismic Hazard Assessment of Lisbon (Portugal). *GeoHazards* **2024**, *5*, 932–970. [CrossRef]
67. Teves-Costa, P.; Batlló, J.; Matias, L.; Catita, C.; Jiménez, M.J.; García-Fernández, M. Maximum intensity maps (MIM) for Portugal mainland. *J. Seismol.* **2019**, *23*, 417–440. [CrossRef]
68. Quintero, J.; Gomes, R.C.; Rios, S.; Ferreira, C.; Viana da Fonseca, A. Liquefaction assessment based on numerical simulations and simplified methods: A deep soil deposit case study in the Greater Lisbon. *Soil Dyn. Earthq. Eng.* **2023**, *169*, 107866. [CrossRef]
69. Geyin, M.; Maurer, B.W. U.S. National VS30 Models and Maps Informed by Remote Sensing and Machine Learning. *Seismol. Res. Lett.* **2023**, *94*, 1467–1477. [CrossRef]